Received: 16 October 2023 | Revised: 7 August 2024 | Accepted: 8 September 2024

DOI: 10.1002/eqe.4237

WILEY

RESEARCH ARTICLE

SSI-induced seismic earth pressures on an integral abutment bridge model: Experimental measurements versus numerical simulations and code provisions

Gabriele Fiorentino[1,2] | **Raffaele De Risi**[1] | **Flavia De Luca**[1] | **George Mylonakis**[3,1] | **Bruno Briseghella**[4] | **Camillo Nuti**[5] | **Anastasios Sextos**[1,6]

[1]School of Civil, Aerospace, and Design Engineering, University of Bristol, Bristol, UK

[2]CNR-IGAG, Institute of Environmental Geology and Geoengineering, National Research Council, Rome, Italy

[3]Department of Civil and Environmental Engineering, Khalifa University, Abu Dhabi, UAE

[4]College of Civil Engineering, Fuzhou University, Fuzhou, China

[5]Department of Architecture, Roma Tre University, Rome, Italy

[6]Department of Civil Engineering, National Technical University of Athens, Athens, Greece

Correspondence

Gabriele Fiorentino, Department of Civil Engineering, University of Bristol, Bristol, UK.

Email: gabriele.fiorentino@bristol.ac.uk; gabriele.fiorentino@cnr.it

Funding information

H2020 Marie Skłodowska-Curie Actions; Horizon 2020 Framework Programme

Abstract

Integral abutment bridges (IABs) generate strong soil–structure interaction (SSI) effects due to their high structural stiffness and transmission of inertial and thermal loads generated at the deck directly to the abutments. Despite an increasing number of experimental and numerical studies available in the literature, there is a lack of consolidated methodologies to model dynamic SSI phenomena for IABs, particularly in seismic regions where uncertainties associated with the induced ground motions render the problem harder to tackle. This study proposes an advanced strategy to model the seismic response of IABs, accounting for dynamic interaction between the structure, the abutment and the foundation, including piles and earth retaining walls. To this end, detailed finite-element studies were carried out employing OpenSees to simulate a recent experimental campaign on a scaled IAB model in a soil container (SERENA) carried out at EQUALS Lab, University of Bristol, in the framework of SERA/H2020 project. An extensive dataset in terms of recorded accelerations, displacements, strains and settlements are available from these tests, including earth pressures which are back-calculated from bending strain measurements. The objectives of this paper are threefold: firstly, the model parameters are explored and assessed critically by comparing the results from the numerical simulations against the experimental data; secondly, once the model is deemed sufficiently representative of the experiments, earth pressures are obtained numerically, as these are not directly measured in the tests; thirdly, the estimated static and dynamic earth pressures on the abutment wall are compared with the predictions of two simplified analytical procedures currently under consideration for inclusion in the new Eurocode 8. The results indicate that records and predictions match well for frequencies of up to 40 Hz at model scale (about 8 Hz in prototype scale) and confirm that the proposed modelling strategy can be used in practical applications. The quasi-elastic model proposed in this study is shown to provide dependable predictions for cases involving moderate strains in real-life applications.

KEYWORDS
earth pressures, Eurocode 8, integral bridges, numerical simulation

1 INTRODUCTION

Integral abutment bridges (IABs), often referred to as jointless bridges, are becoming increasingly popular in many countries being used mainly as highway bridges, overpasses,[1,2] and even railway bridges — primarily in Japan[3] and Germany.[4] IABs are characterised by the absence of joints and bearings between the abutments and the bridge superstructure, leading to a stiff monolithic structure. This is done mainly to minimise construction and maintenance costs (including the substitution of joints and bearings due to fatigue), thus avoiding sustained road closures and traffic interruptions. Moreover, their enhanced redundancy prevents the risk of unseating, a common collapse mechanism of conventional bridges in seismically prone areas (e.g., Ref. 5). On the other hand, thermal stresses, which are aggravated by the absence of joints, can induce damage on the abutments, especially for long spans, so regulations typically prescribe upper limits in the maximum allowable length for such structures (e.g., Refs. 6, 7).

Under seismic excitation IABs generate complex dynamic soil–structure interaction (SSI) effects since, due to the lack of joints and bearings, the response of the deck, abutments and embankments are strongly coupled. Moreover, the dynamic action on one abutment is influenced by a combination of inertial actions imposed by the bridge deck and the backfill thrust against the other abutment.

Earth pressures exerted on abutments can naturally help resist earthquake forces. Still, they can also act detrimentally by operating like masses attached to the structure, thereby increasing the internal forces and deformations.[8] Due to the above ambiguities, many codes, most of which apply to non-seismic regions, provide guidelines for estimating the design forces, especially passive- and active-like static earth pressures on the abutments. For example, the UK PD 6694-1[7] guidelines identify two possible methods of analysis for IABs: Limit Equilibrium methods and Soil–Structure Interaction. In the latter case, the soil is modelled explicitly using finite elements to capture the interaction with the structural system as accurately as possible. As the method requires considerable computational effort, the general practice among bridge designers is using two separate numerical simulations, different for the structure and the soil, thus complicating the design process.[9,10]

In seismically prone areas, there is still a notable lack of consolidated design procedures to evaluate earth pressures behind integral abutments due to the complex dynamic interplay between the IAB and the embankment. The most widely employed simplified method is based on the historical Mononobe–Okabe (M–O) equations[11,12] and their variants, that can only provide a rough, often unrealistic, estimate of the earth pressures along the stem of the wall. M–O is based on the hypothesis of Coulomb's earth pressure theory which assumes that the backfill reaches an ultimate plastic limit state and fails as a rigid wedge sliding along a planar failure surface. Besides ignoring SSI effects, M–O and Coulomb's theories involve exclusively forces (not stresses) so they cannot predict earth pressure distributions along the abutment and, hence, the elevation of the overall soil thrust. In IABs, the movement of the upper part of the wall is restrained by the superstructure, so the backfill does not typically reach an ultimate limit state, especially under passive conditions.[13–17]

An updated version of Eurocode 8 is currently in the process of approval, including some major advancements with respect to the current version.[18] The new draft of Eurocode 8 Part 2 'Bridges'[19] goes beyond the current general guidelines to consider SSI by providing specific rules for IABs, including the interaction between the foundation, the backfill and the abutment wall. In this context, the seismic analyses of IABs should be carried out using a Force- or Displacement-based approach, which is detailed in the Code. In the description of the Force-based approach, particulars are also provided on calculating the total (i.e., static plus seismic) earth pressures.

Regarding the seismic behaviour of IABs, different simplified models have been employed to study the relevant SSI effects. Length limitations were introduced by Frosch et al.,[20] who carried out dynamic analyses in time domain on 2D Finite Element (FE) models by varying the total length of the bridge and the number of spans, and modelling the soil using a series of independent nonlinear springs. Nonlinear dynamic analyses using 3D FE models were employed by various researchers using established software such as OpenSees (e.g., Refs. 21–23) or SAP2000[24] (e.g., Refs. 25–27) with the main scope of obtaining maximum displacements and bending moments on the abutments and piles. In an extensive report, LaFave et al.[28] identified the most vulnerable areas of the bridge and defined limit states for IABs. Dicleli and Erhan[29] investigated the effect of foundation soil stiffness on the seismic performance of IABs. Marchi et al.[30] reported on a time-domain analysis of a simplified soil-bridge model developed in OpenSees, in which the method proposed by Franchin and Pinto,[25] based on distributed nonlinear springs acting between (1) the soil and the abutments and (2) piles, is generalised. Further, Marchi et al.[30] compared their results against those of a sophisticated 3D model of a real IAB-SSI system that enabled validation of the simplified model. Based on these numerical models, the same authors proposed in a more recent paper,[31] two equivalent static models using linear elements and soil springs. Gallese et al.[32] investigated a case study of a single-span integral bridge including SSI using OpenSees, and then used the results to validate a simplified design procedure. The simplified analytical formulations included in Marchi et al.[30] and Marchi and Franchin[31] are currently under consideration for inclusion in the new Eurocode 8 on bridges.

A limited number of numerical investigations focus on the estimation of seismic earth pressures. Mitoulis et al.[33] highlighted the beneficial effect of various mitigation strategies on the response of IABs in terms of earth pressures. To this end, a 2D model was developed for a single bridge abutment constrained at the top by a horizontal elastic spring (i.e., not modelling the entire bridge), including interface elements between the wall and soil. Tsinidis et al.[34] identified the benefits of such improvement strategies by modelling a three-span concrete IAB in 2D, including SSI. Soil–structure interface was modelled using a finite sliding hard contact interface in this case. Xu and Liu[35] carried out numerical analyses on a single-span, full-height integral abutment bridge model on shallow foundations. The interface comprised thin elements interposed between the backfill and the abutments. Xu and Liu also investigated the role of compressible inclusions highlighting a reduction in earth pressures and an increase in bending moment and displacement on the abutments. An increase in earth pressures was also observed as a function of the bridge deck mass. Finite Difference Method (using FLAC software) was used by Seid-Karbasi and Fernando[36] to obtain dynamic earth pressures on a two-span IAB in Ontario, Canada, adopting soil springs between the bridge and the soil. Although some of the aforementioned dynamic numerical models are rigorous, they lack validation against laboratory experiments or field measurements on real bridges. Comparisons between numerical and experimental earth pressures are reported only for static and quasi-static conditions, focusing mainly on the detrimental effects induced by thermal loads (e.g., Ng et al.,[37] Muir Wood and Al-Qarawi et al.[38–46]). Equally, there is a notable lack of numerical studies of IABs focusing on seismic earth pressures validated by experimental data. A recent work by Fiorentino et al.[47] reported on the results of an experimental campaign (SERENA) on a scaled integral abutment bridge model in a soil container focusing on seismic SSI effects. The tests were conducted at EQUALS laboratory, University of Bristol, in the framework of the SERA/H2020 project, with the aim of shedding light on the seismic response of IABs and exploring the effectiveness of two mitigation strategies against earth pressures: the release of pile caps from the foundation and the use of compressible inclusions behind the abutments. An extensive set of probes installed on the model recorded accelerations, displacements and strains, while the earth pressures were back-calculated from bending strain data.

In this paper, a 2D finite-element model of the experimental setup is developed in OpenSees, including the soil domain and featuring advanced strategies to model soil–structure interaction. After a brief description of the experimental campaign, the main features of the numerical model are presented with an emphasis on SSI. Then, a set of numerical results in terms of accelerations, displacements and strains are reported, showing good agreement with the measured data and allowing validation of the numerical model. In a further step, the model is used to obtain an estimate of the static and dynamic earth pressures behind the abutments, which are compared with the predictions of the analytical procedure suggested in the new Eurocode 8 draft, highlighting the importance of a proper evaluation of earth pressures close to the deck-abutment connection. A remarkable finding is that the relatively small strains induced on the physical model allow the development of a high-fidelity quasi-elastic model capable of capturing the recorded accelerations very closely, leading to a dependable characterisation of the soil–abutment wall interface.

2 | DESCRIPTION OF THE EXPERIMENTAL SETUP

The experimental campaign of SERENA project has been discussed in detail in a previous publication.[47] Herein, only the main features relevant to the shear stack (i.e., flexible soil containment box), the physical IAB model and the instrumentation are presented. The sequence of tests, influencing the behaviour of the rig, is also briefly described. The physical model of the integral bridge, displayed in Figure 1, was placed into the soil container of EQUALS Lab as follows: first, four rows of piles were placed in the shear stack, and a first soil layer with a height of 0.4 m, made of Leighton–Buzzard sand fraction B[48] was pluviated. The bridge model, realised in aluminium alloy plates and steel (deck beams), was mounted

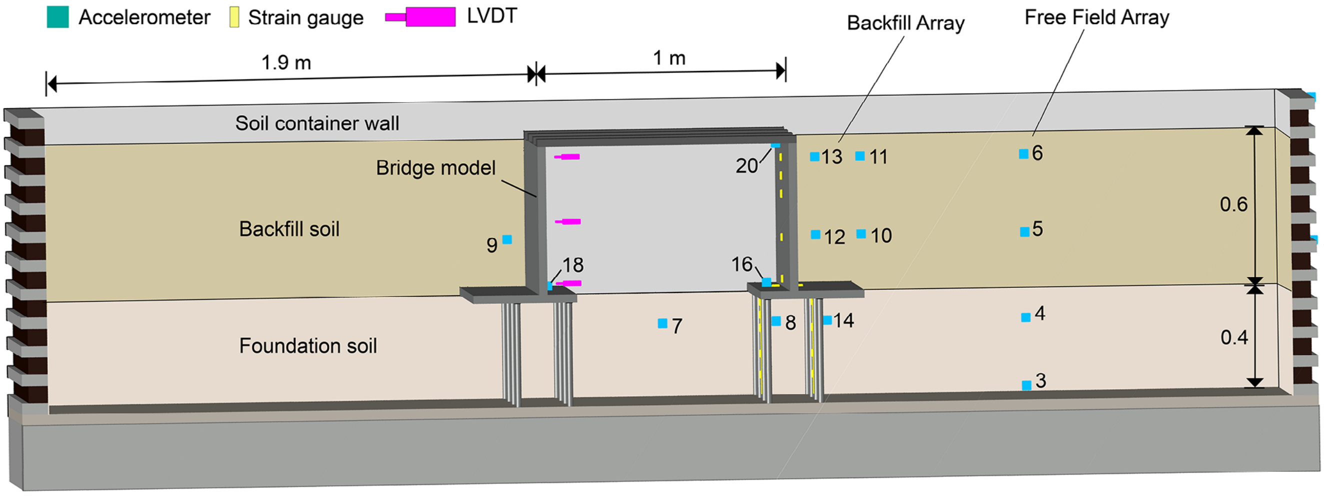

FIGURE 1 Experimental setup and instrumentation layout. Number of channels are reported for accelerometers only. All dimensions in m. The soil domain represented in the numerical model is 4.8 m long and 1 m deep. More details on the rig can be found in Fiorentino et al.[47]

on top of the foundation layer, and the piles were connected to the footings with bolts and nuts. The pile tips were placed into a plywood plug at the bottom of the shear stack, resting on a disk-shaped piece of Polyurethane foam to allow for vertical motion and, thereby, rocking of the pile cap during shaking. Then, a layer of sand was pluviated behind the two abutments, with a backfill height of 0.6 m and a total soil depth of 1 m.

A total of 60 sensors were employed including 24 accelerometers, 32 strain gauges and four Linear Variable Differential Transformers (LVDTs) to measure the response of both the bridge and the soil. The accelerometers (18 horizontal and 6 vertical) were installed at the base of the shaking table and on the western wall of the shear stack, Figure 1. A free field array of four horizontal accelerometers was installed halfway between the external wall of the shear stack and the bridge abutment. Another group of four horizontal sensors was installed in the backfill. Seven accelerometers (three horizontal and four vertical) were mounted on the bridge, while three more were installed close to the piles in the foundation soil. Due to the limited number of channels available in the data acquisition system, most instruments were mounted on the western side of the shear stack. This positioning was made possible by the symmetry of the system which allowed for dense instrumentation on one side only.

Ten strain gauges were installed in the central part of the abutment stem wall and four on the footing. Only two piles were instrumented (Figure 1) using a total of 18 sensors (10 and 8 sensors in the first and second pile, respectively). On the wall with no strain gauges (eastern side), 3 horizontal and 1 vertical LVDTs were also installed to monitor the displacements.

As one of the purposes of the study was to explore the beneficial role of applying foam layers behind the abutments, five different configurations were investigated by varying the number of foam layers between 0 and 2. Different connections between the pile cap and the foundation (i.e., connected or released) were studied. For the first three tests (where piles are rigidly connected with the cap), the testing sequence was EPS2-CP, EPS1-CP, noEPS-CP (i.e., two layers of foam and connected piles, one layer of foam and connected piles, no foam and connected piles, respectively—see Fiorentino et al.[47]). At the end of the testing sequence for each particular configuration, the backfill was excavated down to the base of the abutment to remove the foam layers behind it. The sand was then pluviated back into the emptied area and the tests were repeated for the subsequent configuration. It is worth noting that the bottom (foundation) soil layer and the piles, as well as the portion of the soil, including the free field array, were not affected by these operations. The results presented herein correspond to the reference configuration noEPS-CP, which has no foam layers installed behind the abutments, and the pile heads are connected to the foundation. It is only for studying the response of the piles that a foam-base (EPS2) configuration is used – see Section 4.4. This configuration was chosen as a benchmark because it is most common in prototype IABs. Moreover, the presence of foam layers and the degree of constraint associated with the pile release increases the uncertainty in the earthquake response, thereby it was deemed less suitable for the numerical validation pursued herein with the aim of predicting earth pressures.

The ground motions used in the tests were extracted from the European Strong Motion Database[49] focusing on Italian seismic stations (Cascia, Sellano, Amatrice) soil class B and different acceleration intensities based on three different return periods (T_R), namely 50, 100 and 500 years. The ground motions were matching, on average, the 5% damped

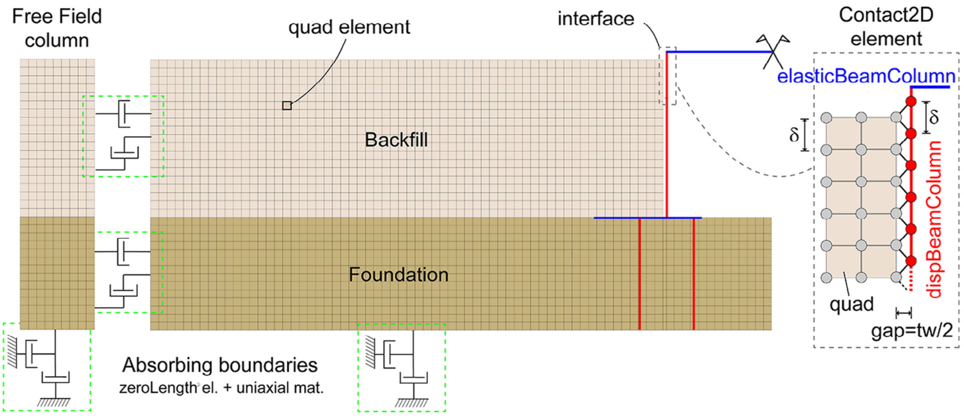

FIGURE 2 2D finite element model implemented in OpenSees/STKO with details of the elements used.

response spectra without scaling the amplitude of the records as per Eurocode 8 spectral matching provisions. The records were scaled in time by a factor of $\lambda_t = 5$ ('time compression') to account for the higher natural frequencies of the scaled physical model relative to the prototype considering a geometric scaling factor of $\lambda = 10$. In addition, to define a 'bedrock motion' as input to the shaking table, the above records were deconvoluted using equivalent linear analysis[50] – a justified simplification in light of the moderate soil shear strains that did not exceed approximately 5×10^{-4}. In this work, we consider only horizontal ground excitations S1, S3, S4 (corresponding to a return period of $T_R = 50$ years), S5 ($T_R = 100$ years), S6 and S7 ($T_R = 500$ years) with PGA values of 0.12, 0.08, 0.14, 0.16, 0.53 and 0.4 g, respectively. In each configuration (e.g., noEPS-CP), the earthquake records were applied in a sequence. Intermediate exploratory white noise signals W1, W2, W3, W4, with a frequency bandwidth 0–100 Hz and $0.005 \times g$ of root mean square acceleration, were applied between successive seismic tests to investigate the dynamic properties of the rig.

3 | NUMERICAL SIMULATION OF SHAKING TABLE TESTS

3.1 | Numerical model

Despite some simplifications as to the material behaviour of the soil, the modelling strategy adopted in this work includes a number of state-of-art techniques which are often employed in cutting-edge software such as ABAQUS,[51,52] FLAC[36] and OpenSees (e.g., Refs. 53, 54).

The aim of the numerical model is to reproduce the response of the experimental setup ('modeling the model' approach), so the dimensions adopted are those of the physical model (see Figure 1). The open-source finite element (FE) platform OpenSees[55] was adopted for the simulations. Different element types were used to represent the superstructure, piles, soil and the interface elements (Figure 2): (a) elastic beam-column elements for the deck beams and the footings; (b) displacement-based beam-column elements for the abutments and the piles; (c) 2D brick Quad elements for the soil and the free-field soil columns; (d) Contact2D elements[56] for the interface between the abutments and soil domain and (e) zero-length elements to connect the free-field columns to the main soil domain.

The mesh of the bridge–foundation–soil system was defined in 2D, considering the plane deformations (plane strain condition) of the tested physical model, which was excited along a single axis. The 2D mesh, including 6502 nodes and 7666 elements, was generated and visualised using the pre/postprocessor software STKO.[57] A TRBDF2[58] solution scheme with Newton–Raphson with line search iteration (error tolerance $\varepsilon = 10^{-4}$ and time step $\Delta t = 1.952 \times 10^{-3}$ s) was adopted in the analyses. Under the hypothesis of small strains and displacements, and non-linear interfaces (see description below), the numerical model, including the abutment and piles, is deemed to behave as a quasi-elastic object (see Section 3.2).

The materials characterising the bridge model, footings and piles (i.e., aluminium and steel) were modelled as Elastic Isotropic. The four steel bridge deck beams (with $\gamma_{st} = 78.5$ kN/m^3, $E_{st} = 210$ GPa, $\nu_{st} = 0.3$) are modelled as an elastic beam-column with a length of 1 m subdivided into 32 elements and a section with a width of 0.4 m and thickness of 0.03 m. The abutments (modelled with 21 elements), footings and piles (14 elements) used aluminium properties ($\gamma_{al} = 27$ kN/m^3, $E_{al} = 69$ GPa, $\nu_{al} = 0.3$). It is noted herein that considering the self-weight of the materials is important as the simulations are non-linear. The discretisation of the structural elements matches the FE mesh of the soil domain. All the constraints

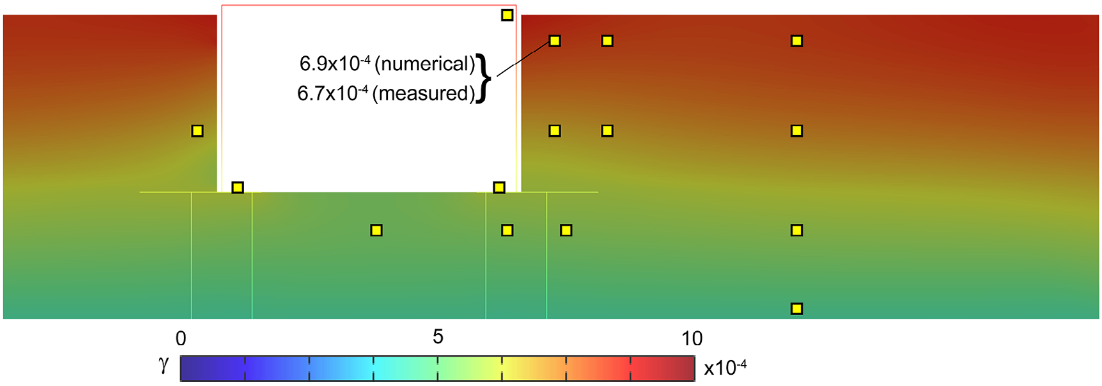

FIGURE 3 Contour map (numerical results) of the peak shear strains derived by dividing the velocities obtained with the OpenSees model by $V_S = 105$ m/s.[14,64] Yellow square markers indicate the position of the accelerometers. Sample maximum values (numerical and measured) are also reported for channel 13 (see Figure 1).

between the different components of the bridge were considered fixed, including the connection between the piles and the footings (pile cap). The bridge abutments were modelled as displacement-based beam-column elements with a height of 0.57 m, width of 0.95 m and thickness of 0.032 m.

The interface between the abutment walls and the soil was realised by means of beam-to-node contact2D (C2D) elements.[56,59,60] These elements define a tensionless-frictional interface between the beam element (abutment) and the soil nodes, allowing for separation between abutment and soil as well as sticking and slipping using a regularised Coulomb law. The width of the abutment wall is represented in the model by a slightly modified geometry, where the distance between the soil elements and the axis of the beam-column element is half the abutment wall thickness (i.e., 0.016 m), thus creating a gap between the beam-column element and the soil to represent the constant width of the abutment wall.[61] In addition, the beam-column element nodes are modelled so that each one falls in the middle of each soil quad element (see Figure 2). In OpenSees, the C2D material is assigned to the C2D elements, defined by two main parameters, namely the interface frictional coefficient μ and the interface stiffness G_i. The parameters of the C2D elements were chosen as $\mu = 0.3$ and $G_i = 10^8$ kPa. The value of μ was selected according to available studies on friction coefficients for piles in contact with Leighton–Buzzard sand.[62] Footings were modelled as elastic beam-column elements with a section width of 0.95 m, depth of 0.4 m and thickness of 0.032 m. The 16 aluminium foundation piles were also modelled as displacement-based beam-column elements. A boundary release was assigned at the pile tips to allow for vertical displacement and, therefore, rocking of the abutment.

Since the model deforms in plane strain mode, for each of the four pile rows a 1- m-long rectangular plate was defined for each row. To derive the plate thickness, the flexural stiffness of the piles in the real three-dimensional case (D_{3D}) was set equal to the one under plane strain condition (D_{2D}). To this end, the flexural stiffness of a plate[47,63] with thickness t_w was employed, defined as (see Figure 3A):

$$D_{2D} = \left[E_p / \left(1 - \nu^2\right)\right] t_w^3 / 12 \tag{1}$$

where E_p is the elastic modulus of the piles and ν is the corresponding Poisson's ratio. On the other hand, the flexural stiffness of a single hollow pile in three dimensions is:

$$D_{3D} = (\pi/64)\, E_p \left(d^4 - d_i^4\right) / B \tag{2}$$

where d and d_i are the external and internal pile diameters, respectively, and B is the width of soil considered (in the analysis at hand, B is the width of the shear stack). By equating D_{2D} and D_{3D} for a row of n piles and considering the material properties to be identical in the two cases, the resulting equivalent wall thickness t_w is:

$$t_w = \left\{ \frac{3}{16} n\, \pi / B \cdot \left(1 - \nu^2\right) \cdot \left[d^4 \cdot \left(1 - \left(d_i/d\right)^4\right)\right] \right\}^{1/3} \tag{3}$$

A similar formulation has been proposed by Ochmański et al.[65] In the present study, the piles have an outer diameter $d = 22.2$ mm, with each row formed by $n = 4$ piles having $B = 1$ m, pile wall thickness $t_p/d = 0.055$ and an internal diameter $d_i = 19.8$ mm. Assuming a Poisson's ratio of 0.3 for the pile, the estimated equivalent thickness of a row of four piles t_w is 5.8 mm. It is noted that ignoring the effect of Poisson's ratio in Equation (3) (as the plane strain condition in the soil container might not be perfectly satisfied), leads to a smaller wall thickness t_w by only 3% − a negligible difference from a practical viewpoint.

The soil domain was modelled using quad elements (FourNodeQuad). To ensure a good resolution of the mesh in terms of captured wavelengths, an upper bound was defined for the element size in the numerical model. This can be evaluated by defining the highest ('cut-off') frequency for the best resolution, computing its wavelength and evaluating the maximum element size. For a cut-off frequency of 100 Hz at model scale, the corresponding minimum wavelength would be $\lambda = V_s/f_{max}= 105/100 = 1.05$ m, where $V_s= 105$ m/s is the minimum shear wave velocity of the system (backfill layer). For a minimum of $N = 10$ elements per wavelength, the maximum element dimension should be $h_{ele} = \lambda/N = 1.05/10 = 0.105$ m. In the numerical model, a finer mesh with element size of 0.03 m was adopted, which amply fulfills this requirement.

The soil material characteristics used in the simulations are those reported in Fiorentino et al.[47] These nominal parameters were estimated from geotechnical tests performed on Leighton–Buzzard sand as part of the SERENA project. They were obtained at the beginning of the experimental campaign without considering the measured response during the tests.

Under the hypothesis of small strains, the soil material was defined as Elastic Isotropic. In accordance with the parameters described in Fiorentino et al.,[47] the values of the Elastic modulus E and the mass density ρ were taken equal to 73 MPa and 1.6 Mg/m^3 for the foundation, and 44 MPa and 1.53 Mg/m^3 for the backfill soil layers. Previous experimental results obtained using the large soil container of EQUALS laboratory resulted in identifying the damping ratio of the SSI system in the range of 3%–6%[66] and around 5%.[15] Therefore, a damping ratio ξ of approximately 6% was assumed and implemented in the numerical model via Rayleigh damping. As will be shown in Section 3.2, this assumption is consistent with the experimental measurements.

Viscous transmitting boundaries[67] are often adopted in numerical SSI formulations to model the unbounded 'outer' medium by introducing dashpots at the boundaries of the mesh to permit the necessary energy radiation and prevent spurious wave reflection. Although the soil container does not generate radiation damping, this modelling strategy was adopted in this study to demonstrate its applicability to real bridges where energy radiation effects are important. At the base of the model, a shear wave velocity $V_R = 400$ m/s and a mass density $\rho_R = 2$ Mg/m^3 were assumed for an underlying half-space, leading to an impedance coefficient $I_R = V_R\, \rho_R\, /\, (V_S\, \rho_S)$ of about 4. This was done to mimic the amplification observed in the experiments, where the shear wave velocity is low ($Vs \approx 100$ m/s) relative to the underlying ground material. This is deemed sufficient to prevent the development of radiation damping at the base of the model.[68–70] When the seismic excitation is defined at the base of the model, an extension of the rig is required (e.g., Refs. 71, 72) so free-field boundary conditions are introduced by defining two elastic free-field columns, connected to the main soil model by means of zero length elements (see Figure 2). Free-Field Boundaries (FFB) are defined by fixing the base nodes, assuming that the underlying material is bedrock, while the other nodes of the FFB are tied together using equal DOF constraints to achieve a simple shear deformation pattern. The shear wave velocity assumed for the sides of the soil container are equal to those of the soil layers (foundation and backfill, respectively).

The Lysmer–Kuhlemeyer (LK) tractions per unit area f_x and f_y can be evaluated[71] for the X and Y directions, respectively as $f_x = -\rho V_p \dot{u}$ and $f_y = -\rho V_s \dot{v}$ where ρ is the mass density of the soil, V_s and V_p are the S- and P-wave propagation velocities of the dry sand and $\dot{u}$ and $\dot{v}$ are the absolute particle velocities in x and y directions. In the numerical model, the velocity-proportional force time-history is applied at the base of the finite element mesh. The assumption of an equivalent linear visco-elastic material for the soil is justified as the soil behaves in a 'stress-strain' regime, i.e., away from failure and where deformations are bilateral, so that equivalent linearity endures.[47] This condition can be verified by evaluating the peak shear strain attained during the experimental tests, that can be evaluated in an approximate manner as 0.2–1.7 times the ratio PGV/V_S,[14] where PGV is the Peak Ground Velocity and V_S is the propagation velocity of shear waves in the soil. The dimensionless multiplier can vary between 0.2 and 1.7, with 1 being a commonly adopted mean value for horizontal ground motion,[64] which is exact for harmonic excitation. Figure 3 shows the contour map of the peak shear strains γ_p evaluated using $V_S = 105$ m/s for the backfill and the velocities computed with the OpenSees model. The maximum values are also reported at 6.9×10^{-4} and 6.7×10^{-4}, for 'numerical' and 'measured' strains, respectively. Evidently, since the amplitude of strains is modest, the soil is away from failure and the assumption of equivalent linearity is justified for interpreting the experimental results.

3.2 | Static and dynamic analyses

In the experimental campaign, the piles were first installed in the soil container, held in position by a wooden jig, then the foundation soil was pluviated to achieve the depth of the pile heads (0.4 m from the container base). Subsequently, the bridge model was positioned and connected to the pile heads. Finally, the soil was pluviated reaching a height of 1 m from the bottom. After testing each configuration, the backfill behind the abutment wall was excavated, allowing the repositioning of the compressible inclusion layers.

The aim of the static analysis in the numerical model was to reproduce these construction steps as accurately as possible. Initial State Analysis in OpenSees allows development of an initial stress field while keeping the original geometry of the problem. First, an Initial State Analysis was carried out by introducing the unit weight of the Foundation soil layer ($\rho = 1.6\ \mathrm{Mg/m^3}$) and the bridge model (the weight of the piles is neglected). This analysis was performed to take into account the gravity analysis of the construction stages before applying the weight of the backfill soil without affecting the geometry of the system. Then, a second gravity analysis with the weight of the backfill soil was performed ($\rho = 1.5\ \mathrm{Mg/m^3}$). The values of ρ for each soil layer were determined by using the measured weight of the sand pluviated at each soil layer and the depth of the layers.[47] Given the non-linear nature of the soil–structure interfaces, establishing the initial stresses is essential for the numerical simulations.

During static analysis, the base of the model is fixed both in x and y directions, and zero friction is assigned along the contact interface between the wall and the soil. During dynamic analysis, the base is fixed for the vertical displacement, the friction is activated along the contact interface; Rayleigh damping and the absorbing boundaries are applied and the dynamic analysis is carried out. The transient analysis is carried using the exploratory white noise (W_i) and the seismic records (S_i) each as a single dynamic analysis.

4 | SIMULATION OF DYNAMIC RESPONSE

4.1 | Fundamental frequency of the system

The numerical modelling strategy described in the previous section was first validated against analytical results. The natural frequencies of a two-layer sand deposit can be derived using available analytical solutions (e.g., Refs. [73–75]). In the numerical model, the shear modulus is assumed constant for each layer. The cyclic natural frequency ω_n can be evaluated according to the Rayleigh equation of Durante et al.[75]:

$$\omega_n^2 = \left[5\, l_1^3 + 5\alpha\left(1 - l_1^3\right)\right]\left[l_1^5\left(3\alpha^2 - 5\alpha + 2\right) + 5\alpha\, l_1^3 (1-\alpha) + 2\alpha^2\right]^{-1} \left(V_{S1}/H\right)^2 \tag{4}$$

where H is the total height of the deposit, $l_1 = h_1/H$ is the dimensionless thickness of the upper layer, $V_{s1} = 105$ m/s and $V_{s2} = 133$ m/s are the shear wave velocities at the base of layer 1 (backfill) and layer 2 (foundation), respectively and $\alpha = \left(V_{s1}/V_{s2}\right)^2$. The resulting analytical natural frequency ($f_{n,an} = \omega_n/2\pi$) is 30.7 Hz. A numerical model of the double-layered soil container full of sand, with a total of 6902 nodes and 7604 quad elements, was modelled in OpenSees, providing an almost identical numerical natural frequency of 30.6 Hz. Both the analytical and the numerical results are consistent with the results obtained during the design process of the shear stack (completely filled with sand), exhibiting a measured natural frequency of about 31.5 Hz for a Leighton–Buzzard Fraction B sand with relative density around 90%.[76] From the cyclic frequency of the deposit and considering low values of hysteretic damping, it is possible to compute the analytical Transfer Function (TF) using the familiar expression[69]:

$$TF(f) \cong \left[\cos^2 F + (F\,\xi)^2\right]^{-1/2} \tag{5}$$

where F is the dimensionless frequency ratio $F(f) = \omega H/V_s = \pi f/2 f_{n,an}$, f is the excitation frequency and ξ is the hysteretic damping ratio of the system. By inverting Equation (5) and knowing the experimental transfer functions, it is possible to back-calculate the damping ratio ξ.

The experimental and numerical transfer functions can be obtained as the ratio of the Cross Power Spectral Density (S_{xy}) to the Power Spectral Density (S_{xx}) for an easier identification of dominant vibration modes[15,77,78]: $T_{xy}(f) = S_{xy}(f)/S_{xx}(f)$. The transfer functions were evaluated using as input the acceleration recorded (or simulated) at the

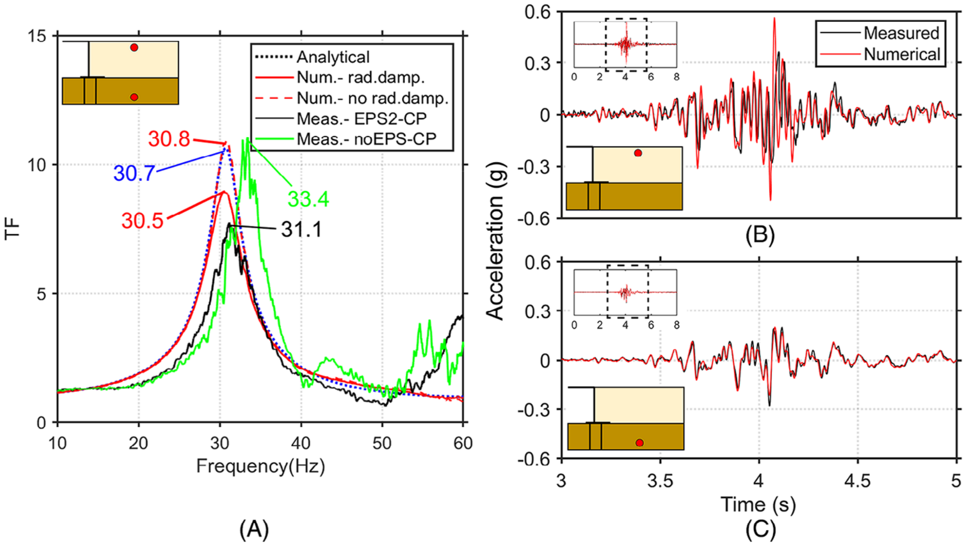

FIGURE 4 (A) Measured and numerical Transfer Functions for Free Field Array (ch3–ch6) sensors under white noise excitation; measured versus numerical acceleration time histories at top (B) and bottom (C) sensor of the free field array zoomed in the interval *t* [3,5] s.

bottom and top of the free field array. The measured frequencies were 34 Hz for W1, 33.4 Hz for W2 and 33.1 Hz for W3 and W4, corresponding to an average uniform damping ratio of 5.3%, 5.8%, 6.3%, and 5.7%, respectively. This is consistent with the damping ratio of 6% adopted in the numerical model. Figure 4A shows the numerical and experimental TFs for white noise W2, in comparison with the analytical transfer function (Equation 5). For the numerical results, two TFs are reported i.e., the model with radiation damping at the box sides and the one without radiation damping (30.5 and 30.8 Hz, respectively). It is evident that the natural frequency is practically the same for the two models, while the amplitude is naturally higher in the absence of radiation damping. The good agreement with the analytical TF is evident in the graphs. The experimental TFs are reported both for the benchmark configuration (noEPS-CP), for which a frequency of 33.4 Hz was obtained, and the EPS2-CP which had a frequency of 31.1 Hz. The better agreement between the numerical results and the latter case stems for this being the first test to be carried out, therefore it likely had a lower density with respect to the benchmark case, which was the third configuration investigated. Overall, the comparison between records and predictions is meaningful.

Regarding the natural frequency of the bridge physical model, the modal analysis in OpenSees of the fixed-base bridge alone displayed in Figure 5A fixed at the level of the pile cap (i.e., without interaction with the foundation and backfill soil), yields a natural frequency at the fundamental mode of 48.3 Hz, Figure 5D. The corresponding frequencies with SSI are obtained by evaluating the transfer function between ch16 and ch20 (bottom and top sensors on the bridge model structure). As contact2D elements impose unilateral constraints, to represent the initial elastic behavior equal DOF constraint was assigned to the wall/soil interface to evaluate the natural frequencies. In Figure 5D, the frequency observed during tests (42.1 Hz) is compared with those obtained with the numerical model for the SSI with the foundation only (Figure 5B) and the full model (Figure 5C), giving 41.3 and 41.8 Hz, respectively – a 15% drop relative to the fixed-base case which is considerable given the strong restraining action of the abutments. The natural frequency of the structure is also evident as a secondary resonance in Figure 4.

4.2 | Acceleration and displacement response

The results in terms of acceleration and displacement time histories obtained using the numerical model match well the experimental data measured in the soil and on the bridge. First, the time series of the acceleration responses recorded during the tests are compared with the simulated ones. Due to the 'compressed' time scale of the records relative to the prototype, the figures of the acceleration and displacement time histories are displayed between 3 and 5 s. In all figures, the measured values are represented with black solid lines, while the numerical ones are displayed with red (record S7) or blue (record S1) lines representing high and low input values of PGA, respectively. Figure 4B,C shows the results for the bottom and top sensors (channels 3 and 6 in Figure 1) of the free field array for record S7. In Figure 4C, at the bottom of

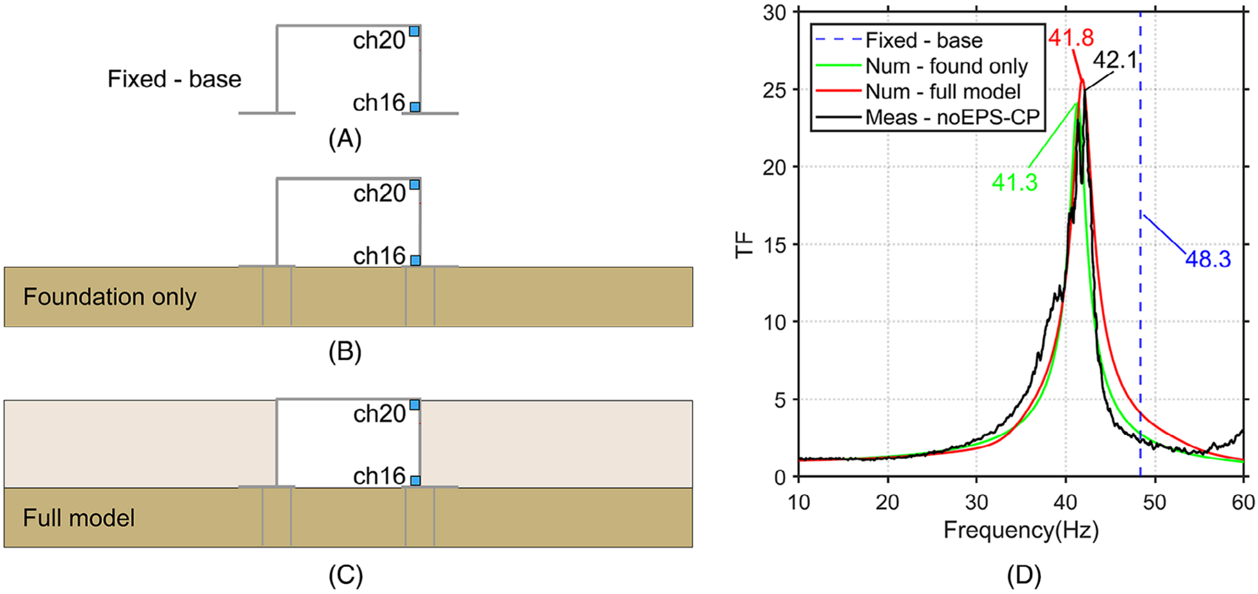

FIGURE 5 Evaluation of the fundamental frequency of the bridge physical model and bridge-SSI system. Left panel: (A) fixed—base model (without SSI); (B) model including SSI with foundation layer only; (C) full model. (D) Measured and numerical Transfer Functions for the different models a, b, c.

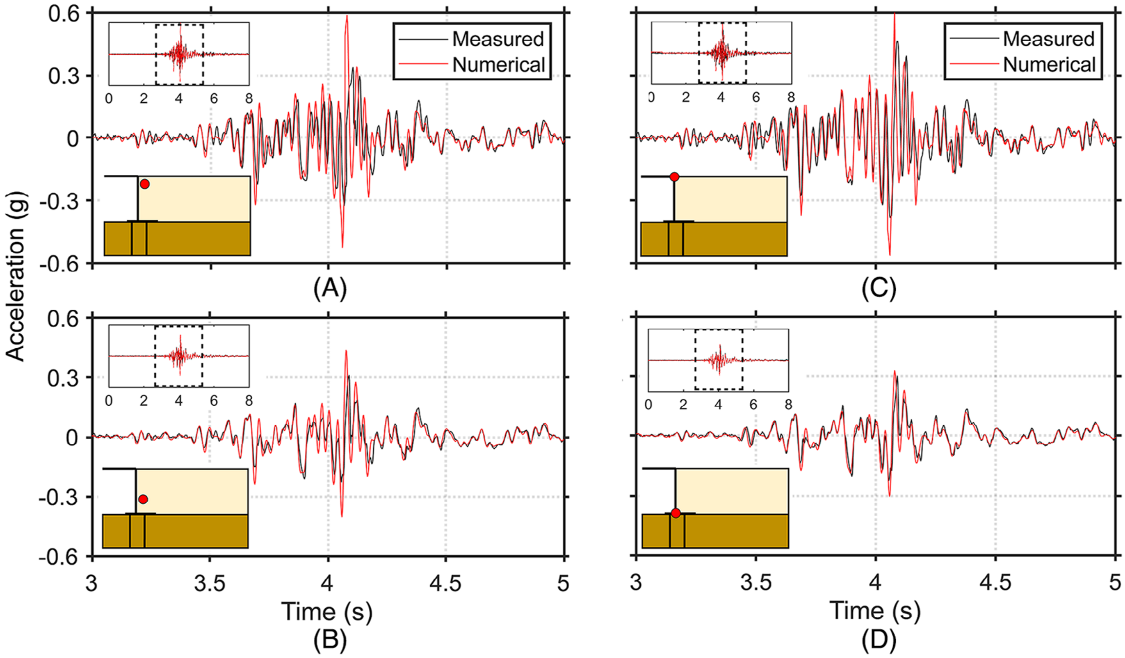

FIGURE 6 Measured versus numerical accelerations on the bridge model for records S7: (A)–(B) backfill array (ch11–ch10) and (C)–(D) bridge (ch20–ch16). Channel numbering is shown in Figure 1.

the soil layer, the numerical values follow accurately the measured values, with the exception of the negative peak which is −0.21 g for the numerical and −0.27 g for the measured data, respectively. In Figure 4B, at the top of the soil layer, the numerical peaks are slightly higher than the measured ones. The main numerical peaks are slightly out of phase with respect to the measures values: the negative peaks happen at 4.06 and 4.07 s with values of −0.49 and −0.28 g, respectively, while positive peaks have a shift of about 0.02 s (4.08 s vs. 4.1 s), and the amplitudes of the first peak are 0.56 and 0.36 g in the numerical and experimental results, respectively.

Figure 6 presents the acceleration responses for the backfill array and on the bridge. The responses of ch10 and ch11 (i.e., Figure 6A,B) are particularly important because of their proximity to the abutment boundary and the contact2D interface.

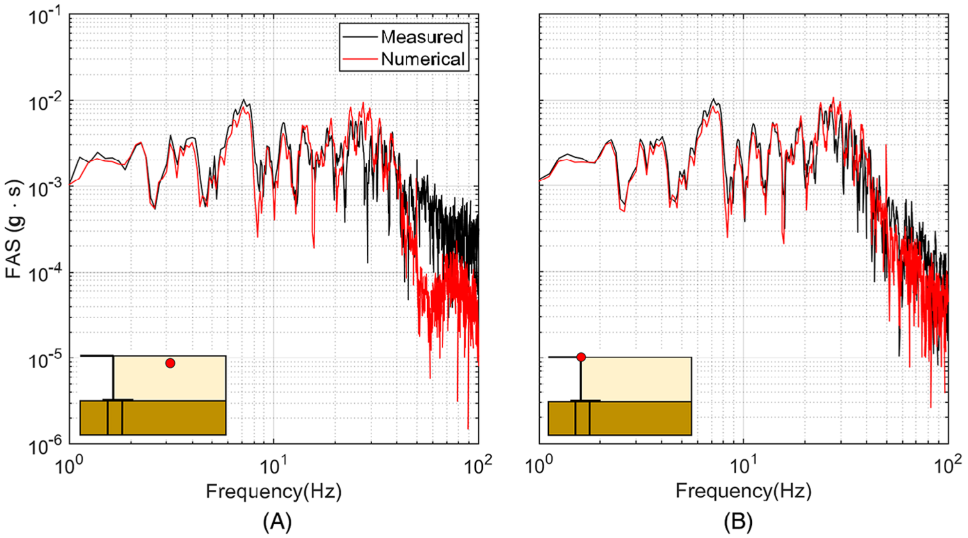

FIGURE 7 Fourier amplitude spectra of measured versus numerical results. (A) Top backfill accelerometer (ch6); (B) top bridge accelerometer (ch20). Note the good agreement between the two curves for frequencies of up to 50 Hz.

Figure 6B, at the bottom of the soil, shows an accurate match with the measured values before and after the peaks, while the amplitudes of the negative peaks are at −0.39 and −0.24 g, and those of the positive peaks are 0.43 and 0.35 g, for the numerical and experimental case, respectively. The match in Figure 6A is also good, with negative peaks reaching −0.52 and −0.35 g, while the positive peaks reaching 0.58 and 0.33 g, for the numerical and experimental data, respectively. Similarly to the results shown in Figure 4B,C, the measured peaks at the top of the soil layer are out of phase by a time shift of 0.02 s. At the bottom of the bridge (see Figure 6D), negative peaks reach −0.3 and −0.22 g, while the positive peaks are at 0.33 and 0.3 g, for the numerical and experimental case, respectively. At the top of the bridge (see Figure 6C), negative peaks at −0.56 and −0.37 g, while the positive peaks are 0.6 and 0.46 g, for the numerical and experimental results, respectively. The match is better for the bottom sensors in the free field, in the backfill soil and on the bridge. In the top sensors, there is also a larger shift between the positive maxima. Overall, the comparisons between recorded and predicted time histories indicate a good match before and after the highest peaks, while the accuracy of the numerical solution deteriorates at locations near the soil surface both for maxima and minima.

The good agreement between the measured and computed accelerations in terms of frequency content is shown in Figure 7, where the Fourier Amplitude Spectra (FAS) are provided for ch6 at the top of the backfill (Figure 7A) and ch20 at the top of the bridge (Figure 7B). The agreement is indeed excellent in the range 1–50 Hz for both cases.

Figure 8 shows numerical results in terms of contour plots of acceleration distributions for record S7, compared with measured values (yellow square markers). Figure 8A illustrates the acceleration values at the times when the acceleration is minimum (negative), which are $t = 4.02$ s and $t = 4.03$ s in the numerical and physical model, respectively. It can be observed that there are some differences in the spatial distribution, but this is expected as the comparison shows data for the same time instant. For example, for ch3, the measured acceleration is equal to zero at $t = 4.02$ s, but this is due to maxima not happening simultaneously at different points. Figure 8B depicts the acceleration values at $t = 4.06$ s and $t = 4.07$ s for the numerical and experimental case, respectively, which are in good agreement. Overall, the experimentally measured traits of the wave propagation throughout the soil domain are well captured in the numerical simulations.

In both cases, there are areas of high accelerations (up to 0.6 g) in the backfill, at the interface between the soil and the abutment just below the deck-abutment connection. This is one of the areas that should be checked carefully in real integral bridges, as it is where settlements and gaps between the abutment, the embankment, and the transition slab are concentrated.[79,80]

Figure 9 shows a comparison of numerical results in terms of relative displacements at the location of the LVDT at the top of the bridge abutment. The results for record S1 (low acceleration input) show maxima of 0.012 and 0.032 mm for the numerical and the experimental case, while the negative minima are −0.016 and −0.034 mm.

For S7 (Figure 9B), the numerical displacements follow the measured ones up until $t = 3.5$ s, where the measured values become higher (0.22 mm compared to 0.11 mm in the numerical model, then −0.17 and −0.1 mm). Evidently, there is a slight shift between the phases (0.01 s) of the displacements. Overall, the relative displacement is smaller in the

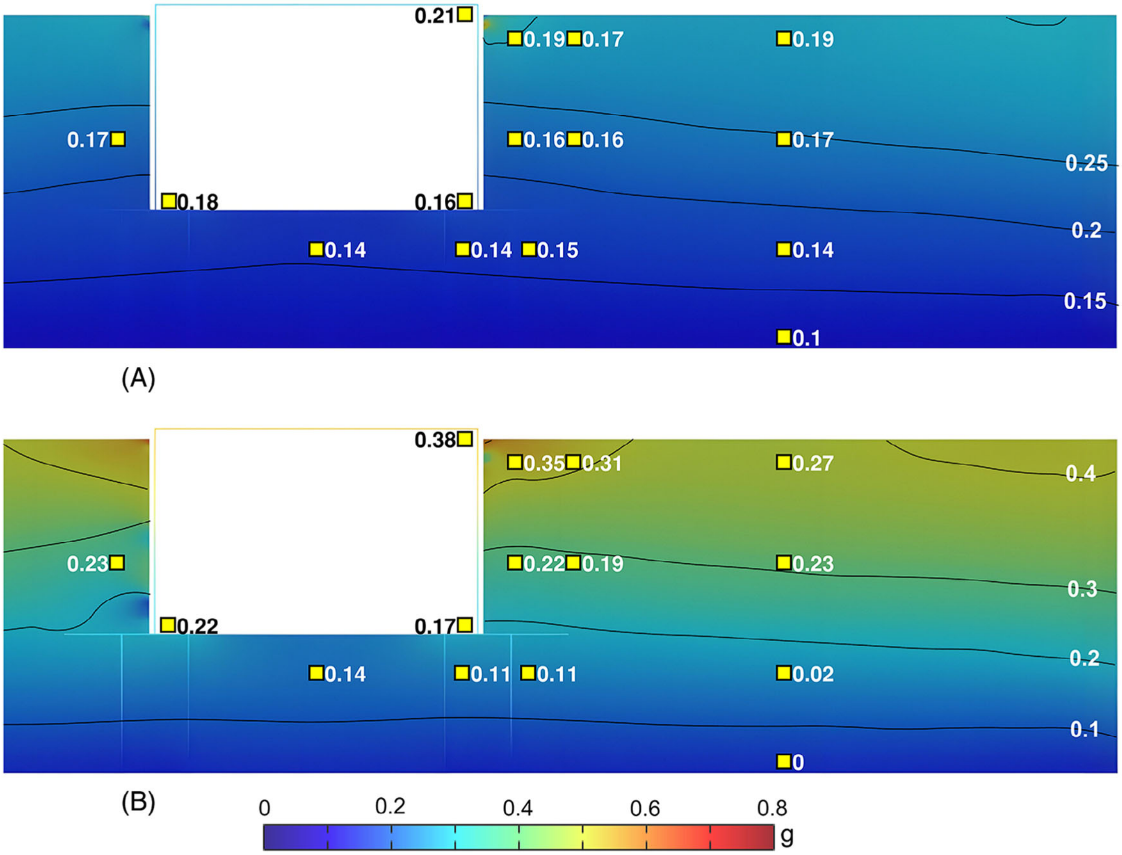

FIGURE 8 Contour plots of accelerations distribution for record S7 along the 2D model versus measured results (zoom on the instrumented part of the soil box) at the instant corresponding to the (A) maximum (step 2079 for numerical and 2083 for measured response) and (B) minimum (step 2061 for numerical and 2063 for measured response). Yellow square markers indicate the position of the accelerometers as shown in Figure 1.

FIGURE 9 Comparison between measured and numerical relative displacement at ch59 LVDT location with respect to ch57 LVDT [top and bottom of the left abutment wall for experimental tests (A) S1 and (B) S7].

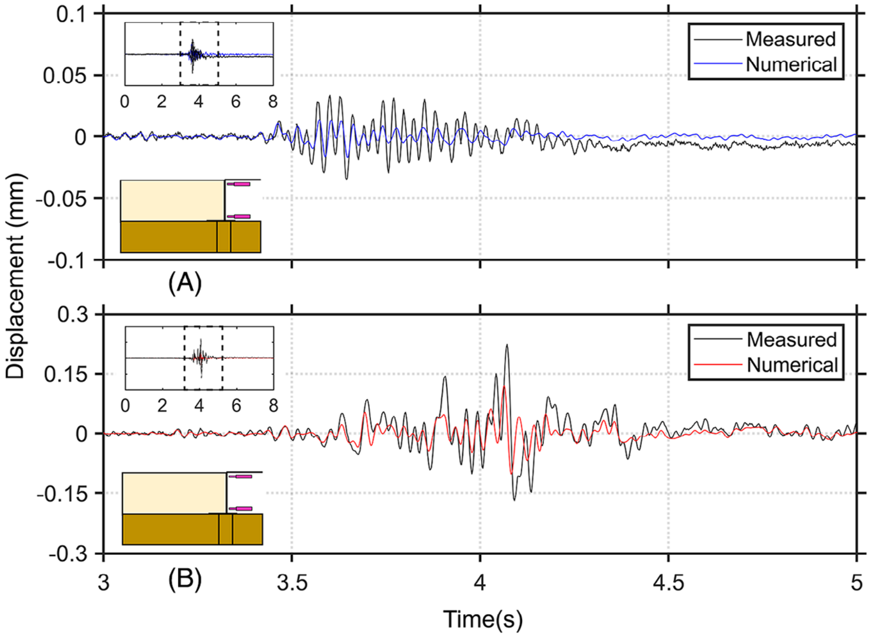

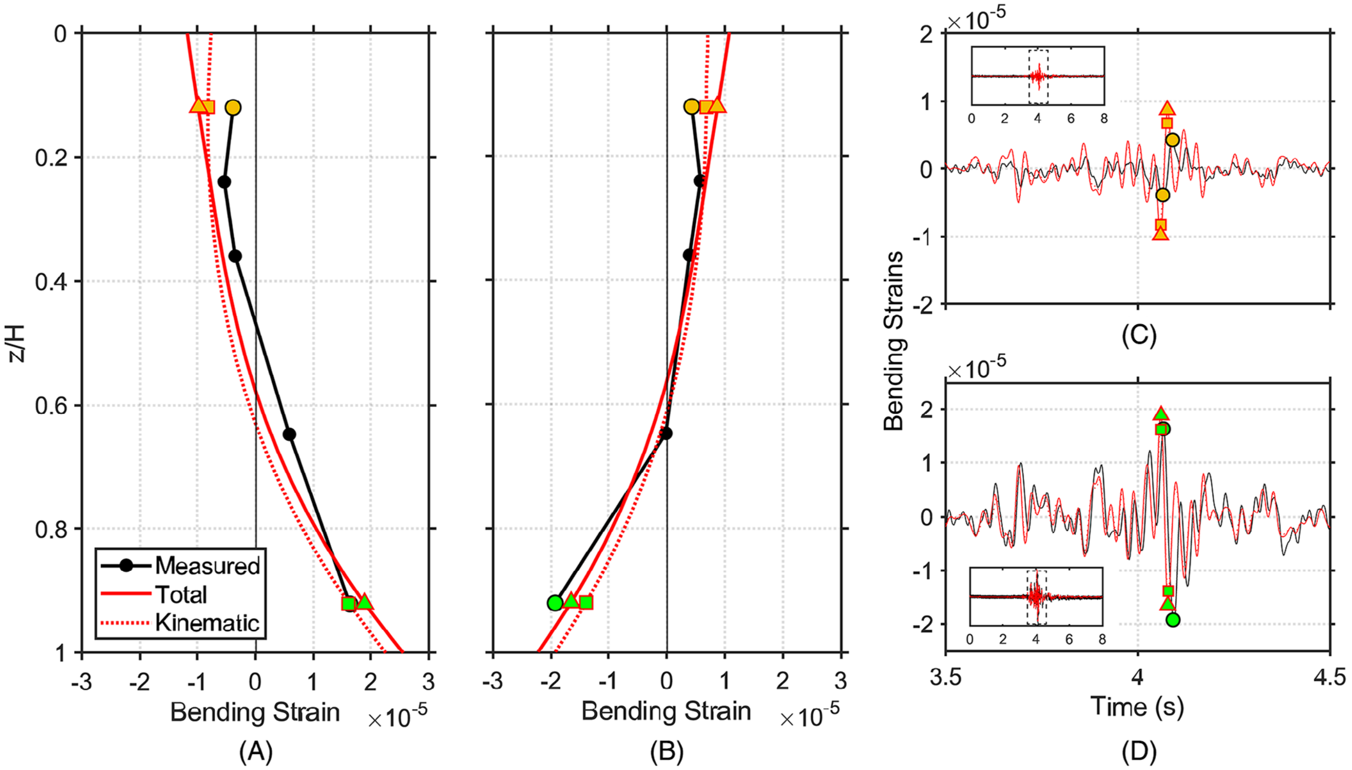

FIGURE 10 Numerical versus recorded responses: maximum bending strains on abutments (A) towards the soil (*t* = 4.06 and 4.07 s for the numerical and measured response, respectively); (B) away from the soil (*t* = 4.08 and 4.09 s for the numerically evaluated and measured responses, respectively).

numerical model relative to the measurements. This is the case for both low (S1) and high intensity accelerations (S7), see Figure 9A,B respectively. This is likely due to the boundary conditions and constraints in the numerical model which result in a less deformable SSI system. The comparison of frequencies in Figure 5B suggests that this is indeed the case, i.e., the natural frequency of the numerical model is slightly higher than the estimated frequency of the physical model, even if the difference is small.

4.3 | Bending strains on the abutments

The results obtained with the numerical model on the abutment wall are compared in Figure 10 with the experimental ones in terms of bending strains. The numerical model captures the trends measured by the strain gauges in the experiments. It is observed that the variation of bending with depth is not hydrostatic and is symmetrical in both directions, following a parabolic-like curve.

Figure 10 displays the bending strains at the time instant of the maximum (towards the soil, Figure 10A) and minimum (away from soil, Figure 10B) versus dimensionless depth z/H, where z is depth and H the height of the abutment wall. In the time histories (Figure 10C,D), it is evident that the peaks are out of phase between the numerically predicted and the measured response. Therefore, in Figure 10A the values are relative to $t = 4.06$ s for the numerical and $t = 4.07$ s for the measured, while in Figure 10B the values refer to $t = 4.08$ s for the numerical and $t = 4.09$ s for the measured.

The influence of kinematic and inertial interaction on the response of the soil–abutment system was investigated in the numerical model by comparing the most complete simulation which includes the deck mass, representing the total response of the soil–abutment system, to a simulation without deck mass (red dotted line), thereby accounting for kinematic response only.

The bending strain response is displayed in terms of time histories for the top and bottom location of the strain gauges with orange and green markers, respectively. The maxima are highlighted with different markers, i.e., circular (measured response), square (kinematic response) and triangular (total response). In Figure 10A, at the top the values of the bending strains are -8.2×10^{-6}, -9.8×10^{-6} and -3.9×10^{-6}, while at the bottom they are 1.62×10^{-5}, 1.89×10^{-5} and 1.6×10^{-5}

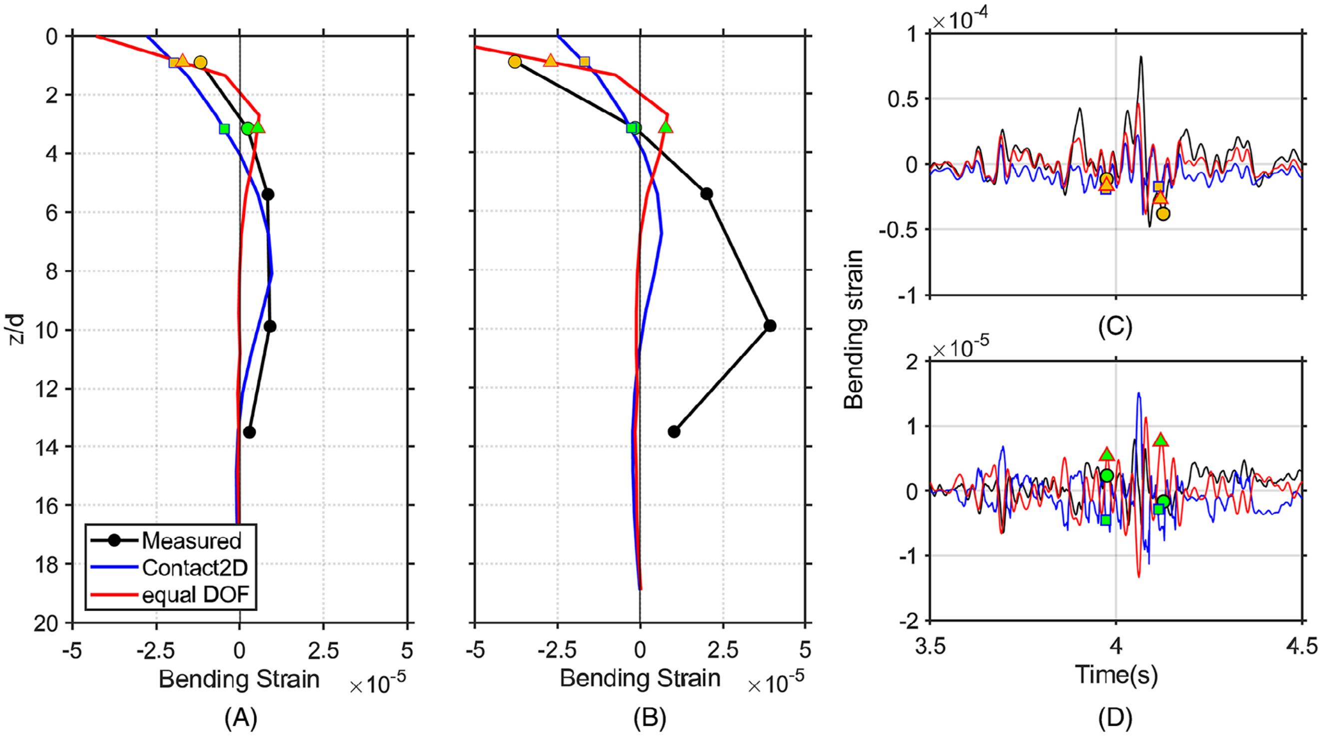

FIGURE 11 Comparison of bending strains on the foundation piles. Bending strain on the left instrumented foundation pile at two instants of the time history response: (A) $t \approx 4$ s and (B) $t \approx 4.1$ s. Measured values, noEPS-CP (dotted black line), numerical—contact2D (light blue line) versus numerical—equal DOF results (red solid line). The highlighted locations indicate those of the top (orange) and bottom (green) strain gauges used for the comparison of bending strain time histories of (C) and (D). Circle, square and triangle markers indicate measured, total numerical and kinematic (i.e., without deck mass) numerical responses.

for the kinematic, total and measured response, respectively. In Figure 10B at the top the values of the bending strains are $6.8 \times \cdot 10^{-6}$, $8.6 \times \cdot 10^{-6}$ and $4.3 \times \cdot 10^{-6}$, while at the bottom they are $-1.4 \times \cdot 10^{-5}$, $-1.65 \times \cdot 10^{-5}$ and $-1.9 \times \cdot 10^{-5}$ for the kinematic, total and measured response. The total response is naturally larger than the kinematic one, while the measured values are lower than the numerical ones at the top and at bottom of the abutment, except for one case where at the bottom the kinematic and measured response attain similar values. This suggests that the actual degree of fixity between the deck and abutment is probably lower than the perfectly encased condition assumed in the numerical model (see Ref. 47).

4.4 | Bending strains on foundation piles

In the experiments, the piles were hollow cylindrical aluminium piles spaced at distances $S = 300$ mm, i.e., the ratio $S/d \approx 13.5$. Therefore, the piles behave as solitary elements rather than as a group.[81,82] Analysing their response requires solving a three-dimensional (3D) problem, while the numerical model proposed in this study assumes plane strain conditions (2D). As a result, in addition to the aforementioned equivalence in terms of flexural pile stiffness in two and three dimensions, the frictional shear tractions developing at the pile-soil interface should be considered. Some authors (e.g., Ref. 65) have proposed methods to include these forces in 2D models, while the trend in geotechnical engineering is to employ simplified Winkler models for considering SSI effects on piles, in which these actions are inherent (e.g., Refs. 83–85). Some commercial software, such as PLAXIS2D,[86,87] convert 3D problems in 2D plane strain numerical models. Despite the considerable number of experimental studies on piles, only a few have investigated the ability of 2D models to reproduce dynamic experimental results, and most commonly discrepancies between measured response and numerical simulations are reported (e.g., Ref. 88). Conversely, there are several studies demonstrating good matching between 3D numerical models and measured results (e.g., Ref. 89) but not for the complex case of abutment-backfill-foundation-subsoil system. A comprehensive discussion on this topic lies beyond the primary scope of this work that focuses on earth pressures.

To compare measured and numerical results on piles, Figure 11A,B shows a comparison between the measured bending strains on the left instrumented pile and the numerical results for noEPS-CP configuration at two different instants, namely 4 and 4.1 s. In addition to the case with equal DOFs condition along the piles (red line), bending strains were also evaluated using a model with contact2D elements along the piles (light blue line), which has the effect of lowering the depth of the maximum bending moments along the pile, while the maximum value at the top decreases. For the numerical results the instants corresponding to the peaks providing a similar shape of the measured response were chosen.

The numerical results with the equivalent thickness of the sheet pile, here denoted as *EI* (see Section 3.1) and with equal DOFs are comparable to the experimental ones at the top, while lower in the pile they are smaller. The comparison with the results obtained by using contact2D elements shows that the point of maximum moment drops from about 2.7 to 7 pile diameters, while the maximum bending strain is not increasing. It can also be observed that at certain instants (e.g., $t \approx 4$ s, Figure 11A) the matching between the measured and the numerical model with contact2D is very good, while in others (e.g., $t \approx 4.1$ s, Figure 11B), measured values are much larger along the pile. Figure 11C,D shows the time histories of bending strains for the location of the top two sensors along the left instrumented pile. Orange and green markers indicate the first and the second sensor from the top, respectively, while the maxima are highlighted with different markers, i.e., circular (measured response), square (Contact2D) and triangular (equalDOFs). At $t \approx 4$ s at the top sensor, the bending strains are $-1.95 \times \cdot 10^{-5}$, $-1.7 \times \cdot 10^{-5}$ and $-1.4 \times \cdot 10^{-5}$, while for the second sensor they are $-4.6 \times \cdot 10^{-6}$, $5.4 \times \cdot 10^{-6}$ and $-2.4 \times \cdot 10^{-6}$ for the contact2D, equal DOFs and measured case, respectively. At t $\approx$ 4.1 s at the top sensor, the bending strains are $-1.7 \times \cdot 10^{-5}$, $-2.9 \times \cdot 10^{-5}$ and $-3.8 \times \cdot 10^{-5}$, while for the second sensor they are $-2.7 \times \cdot 10^{-6}$, $7.6 \times \cdot 10^{-6}$ and $-1.6 \times \cdot 10^{-6}$ for the contact2D, equal DOFs and measured case, respectively.

Overall, it can be concluded that while at certain instants a good matching is obtained, the level of strain of the soil in contact with piles does not match the overall global conditions identified in Figure 3 and requires a bespoke modelling strategy which lies beyond the scope of this study, for which the overall match in terms of maximum strain on top is sufficient to reproduce the measured response.

4.5 | Evaluation of earth pressures according to design-oriented formulae and code provisions

An updated version of Eurocode 8 is currently in the process of approval and will include some advancements over the current version in terms of treatment of SSI effects in IABs. The draft of Eurocode 8 Part 2 ‘Bridges’[19] provides specific rules for integral abutment bridges, including the effects of soil–structure interaction in the analyses which occurs at the foundation and through earth pressures on the vertical abutment wall. The seismic analysis of IABs should be carried out using a Force or Displacement based approach, which are detailed in the code. Two different formulations for the Force-based approach are under consideration for inclusion in the new version of Eurocode 8, as detailed by Marchi[30] and Marchi and Franchin[31] to calculate the total earth pressure E_d (static plus seismic). The pressures E_d approach the active limit on one abutment (i.e., when the abutment wall moves away from the soil, denoted as ‘upstream’) while on the ‘downstream’ side (i.e., when the abutment wall moves towards the soil), the earth pressure is intermediate between the *at-rest* and the *passive* limit.

4.5.1 | Method by INTAB project as modified by Marchi[30]

The specific pressure distribution was adopted from the INTAB project which focuses on thermal loads.[90] According to this method, the total earth pressure along the height of the abutment wall can be calculated as:

$$\sigma_{p,mob}(z) = K_{PE,mob}(z)\,\gamma z \tag{6}$$

where $\sigma_{p,mob}$ is the mobilised passive pressure at depth z measured from the abutment top and γ is the unit weight of the backfill material behind the abutment. $K_{PE,mob}$ is a depth-varying mobilised passive pressure coefficient under seismic conditions that can be evaluated from the following expression:

$$K_{PE,mob}(z) = K_0 + \left(K_p - K_0\right)\, i_u(z) \tag{7}$$

which interpolates between the at-rest pressure coefficient K_0 the passive pressure coefficient under seismic conditions K_p (Refs. 16, 91, Rampello et al.[92]) using the depth-dependent empirical interpolation function $i_u(z)$:

$$i_u(z) = u(z) / [a\, z + u(z)] \tag{8}$$

where $u(z)$ is the horizontal wall displacement at depth z from the abutment top and a is a non-dimensional soil-dependent parameter, equal to 10^{-1} for loose soil (as in this study) and 10^{-2} for dense soil. The method proposed in the above references is iterative, starting from an initial assumption as to the magnitude of earth pressures, then computing the depth-varying wall displacement $u(z)$ using a pseudo-static analysis of a frame model, and then iterating by re-evaluating the earth pressures according to Equations (6)–(8) and so on until an acceptable level of convergence is achieved. As in our case the displacement function $u(z)$ is established directly from 2D FE analysis, no iterations were employed after the passive-like earth pressures were evaluated from the above equations.

Pertinent expressions for calculating seismic passive pressure coefficients K_p are given in Annex F of the draft version of the Eurocode 8 part 5 regarding geotechnical aspects,[93] derived from the formulation proposed by Lancellotta[91] as reported by Rampello et al.[92] Considering $\varphi = 35°$ for the Leighton–Buzzard sand fraction B, a smooth wall and a lateral seismic coefficient $a_h = 0.27$ (corresponding to the PGA of record S7 at table level), this formulation provides a value of $K_p = 3.09$ [equal to the value obtained by the more general formulation by Mylonakis et al.,[16] while the conventional static Rankine passive coefficient is 3.69 and the seismic one using the generalized Rankine solution by Kloukinas and Mylonakis[94] is 3.56.

For a vertical smooth wall retaining a horizontal backfill subjected to horizontal earthquake action, the above values can be obtained by means of the general formulation by Mylonakis et al.[16] via the equations

$$K_p(z) = [1/\cos\psi_e] \cdot [1-\sin\varphi] / [1+\sin\varphi\cos(\Delta_1+\psi_e)] \cdot [\exp(-2\theta_e\tan\varphi)] \tag{9a}$$

$$\sin\Delta_1 = \sin\psi_e / \sin\varphi \tag{9b}$$

$$2\theta_e = -\Delta_1 + \psi_e \tag{9c}$$

$$\tan\psi_e = a_h \tag{9d}$$

in which Δ_1 is the so-called Caquot angle, ψ_e is the inclination of the body force in the backfill, θ_e is the angle separating the major principal planes near the wall and the backfill surface and a_h is the lateral seismic coefficient. Note that the above equation can be used to predict both active and passive earth pressures if the parameters φ, ψ_e and a_h are taken as positive and negative (this study), respectively. The more general equation for a rough inclined wall retaining an inclined backfill is provided in the above publication.

4.5.2 | Method by Marchi and Franchin[31]

According to this method, the total earth pressure along the height of the abutment wall can be calculated as:

$$\sigma_{p,mob}(z) = \begin{cases} K_p \gamma\, z & z \le \Delta H \\ K_p\, \gamma \Delta H & z > \Delta H \end{cases} \tag{10}$$

where $\sigma_{p,mob}$ is the mobilised passive pressure at depth z from the abutment top and γ is the unit weight of the backfill material. ΔH is a critical depth below which earth pressures are constant, defined as:

$$\Delta H = c\, \alpha\, H \text{ with } \alpha = (S_a/g)(w_{deck} L_{tot} + 2\, w_{abut}\, H) / \left(1/2\, K_p\, \gamma H^2 B\right) \tag{11}$$

where L_{tot} and H are the total length of the deck and height of the abutment. The weights per unit length of deck and abutment are denoted by w_{deck} and w_{abut}, respectively, and B is the abutment width. The resulting pressure distribution follows that for passive earth pressures up to a depth ΔH and then attains a constant value.

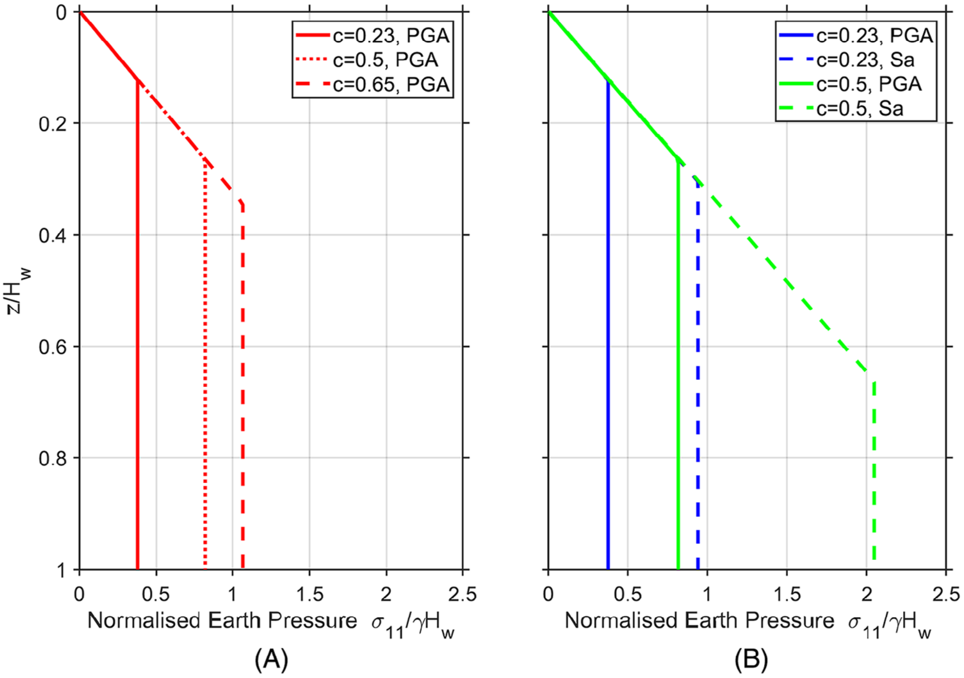

FIGURE 12 Design earth pressures obtained with the formulation proposed by Marchi and Franchin[31]; (A) PGA = 0.274 g, earth pressures for different values of the coefficient $c = 0.23, 0.5, 0.65$; (B) $c = 0.23$, earth pressures for PGA and Sa = PGA × 2.5 as specified for EC8 Type 1 elastic spectral shape.

c is a measure of the abutment-to-foundation relative stiffness and accounts for the portion of inertial forces transmitted to the abutment-backfill system relative to that transmitted to the foundation. c attains different values depending on the configuration of the integral bridge and depends on the number of spans. MF23 suggests values $c = 0.58$ for a single span bridge, while $c = 0.65$ and $c = 0.59$ for two and three spans, respectively. The value suggested in the EC8 draft is 0.5. A lower c value implies that a larger part of the inertial forces is transmitted to the foundation as displayed in Figure 12.

For the physical model at hand, we have evaluated c as the ratio of the total soil thrust on the wall over the sum of the horizontal reaction forces at the two foundations. In particular, the ratio has been evaluated using the algebraic minima and maxima of the two forces at $t = 4.06$ s and $t = 4.08$ s, respectively, obtaining two values of c: 0.18 for the minima and 0.23 for the maxima. As a conservative estimate, we have adopted $c = 0.23$. It should be noted that the resultant of pressures on the abutment wall was obtained by integrating the horizontal (principal) normal stresses σ_{11} over the wall length, while the foundation horizontal reactions were evaluated by summing the horizontal forces transmitted to the plate foundation element (horizontal blue element under the wall stem in Figure 2) from the soil layer above (backfill) and below (foundation), as well as the piles in the OpenSees model. For the complex foundation at hand, this approach was deemed superior over merely considering the internal shear force at the base of the wall stem.

Depending on the acceleration intensity and the value of c, the height at which the earth pressure becomes constant varies considerably. In Figure 12A, the curves for $c = 0.23, 0.5, 0.65$ are given for PGA = 0.274 g (i.e., PGA for S7 input), while in Figure 12B the curves are given for $c = 0.23$, $c = 0.5$ (single span bridge) and two different values of acceleration intensity [PGA, spectral acceleration obtained as the PGA times 2.5 (Sa = 0.685 g) based on EC8 Type 1 spectral shape for the constant acceleration branch in the spectrum].

The bridge model discussed in this paper is made of steel and aluminium (relatively lighter) and has a relatively stiff foundation, made by two rows of piles. This is consistent with the shape of the bending moments in Figure 10: they are smaller at the top and larger at the base. It is important to highlight that the ratio of the soil-wall relative flexibilities for model and prototype remains constant as detailed in the scaling laws suitable for SSI problems.[47]

The resulting dimensionless downstream earth pressures ($\sigma_{11}/\gamma H_w$), plotted against the normalised depth from the wall top (z/H_w), are displayed in Figure 13 (black dashed plot). At rest earth pressures are also shown, evaluated according to Jaky's equation ($K_0 = 1 - sin\varphi \approx 0.43$).

The design thermal earth pressures prescribed for integral bridges by the UK code PD6694,[7] obtained for a temperature change $\Delta T = 50°$C are also reported as a reference (green dashed-dotted line). These earth pressures are equal to the static

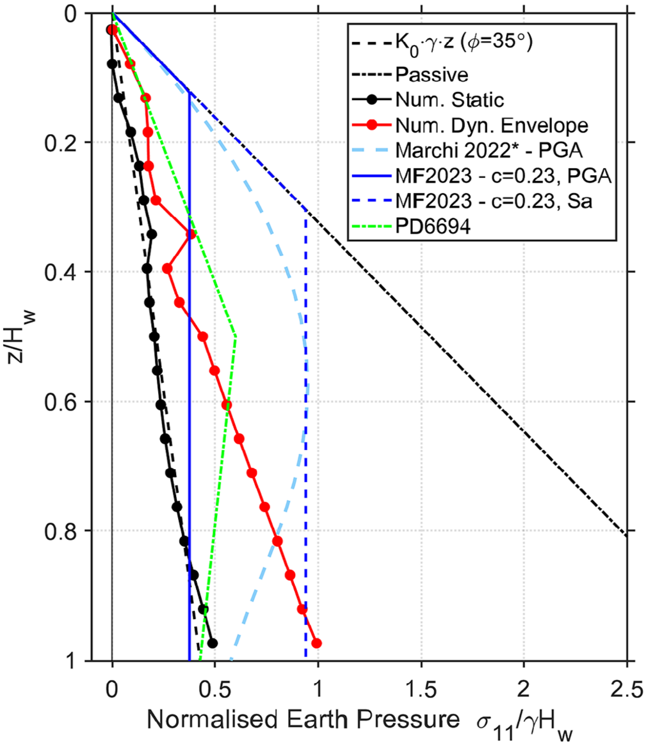

FIGURE 13 Earth pressures behind the abutment wall: total earth pressures at the end of gravity load analysis estimated for PGA = 0.274 g from shaking table input; Sa = PGA × 2.5 as specified by EC8 Type 1 spectral shape[30]; predictions do not employ iterations (indicated as * in the legend); MF2023, Marchi and Franchin.[31].

ones at the bottom of the abutment and attain a maximum value of 0.6 at $z/H_w = 0.5$. The numerical earth pressures (horizontal stress component σ_{11} in OpenSees) were evaluated by averaging the results on the four nodes of each quadrilateral element of the backfill in contact with the abutment wall, so that the result reported refers to the center of each quad element.

Good agreement is observed in Figure 13 between the theoretical *at rest* pressures (black dotted line) and the numerical predictions at the end of the gravity analysis stage (black solid line). The envelope of maxima of total earth pressures (i.e., static plus dynamic) for record S7 (PGA at table level of 0.274 g) is also shown (red solid line). At the bottom, the total pressures are twice as large (1) as the at-rest pressures (0.5). Notably, the results obtained are consistent with the trends of earth pressure obtained by other authors (e.g., Ref. 35). Overall, the design-oriented equations appear to yield results that are closer to the numerical values if *c* is evaluated using the numerical model, while they are consistently on the conservative side if a value of 0.5 is adopted, i.e., the suggested value by Marchi and Franchin[31] to avoid under-design of the foundation.

As it is important to explore the effect of a heavier deck (e.g., the case of a longer deck span) on earth pressures, a numerical study was carried out by doubling the deck weight during static analyses (Figure 14A) and the inertial mass during dynamic analyses (Figure 14B). The additional weight in the gravity analysis increases the static earth pressures behind the wall at depths between 0.1 and 0.6 z/H_w; the maximum normalized earth pressures at $z/H_w = 0.34$ are 0.19 and 0.26 for one and two times the nominal deck weight, respectively.

The effect of additional mass in the results of the seismic analysis (see Figure 14B) is naturally more significant. As can be observed from the envelope of the seismic earth pressure increment with height, the stronger effects are observed in the upper section of the wall (0 to 0.4 z/H_w). It is worth noting that for two deck masses there is also an increase in the bending strains of about 40% and 20%, at the top and bottom of the abutments, respectively. This depth is roughly equal to the 'active length' of the wall which for the specific case is estimated at around 0.5 H_w.[95] In the upper third of the abutment, the earth pressure doubles for the case of two deck masses over the reference case. Note that the first two points for the double-mass deck (Figure 14B) exceed the seismic passive value calculated using K_p – yet this violation can be deemed minor from a practical viewpoint.

Evidently, when the deck span length increases, the changes in static and seismic earth pressures behind the abutment wall can be significant. The influence of the deck length/mass must be taken into account in the design phase, also for

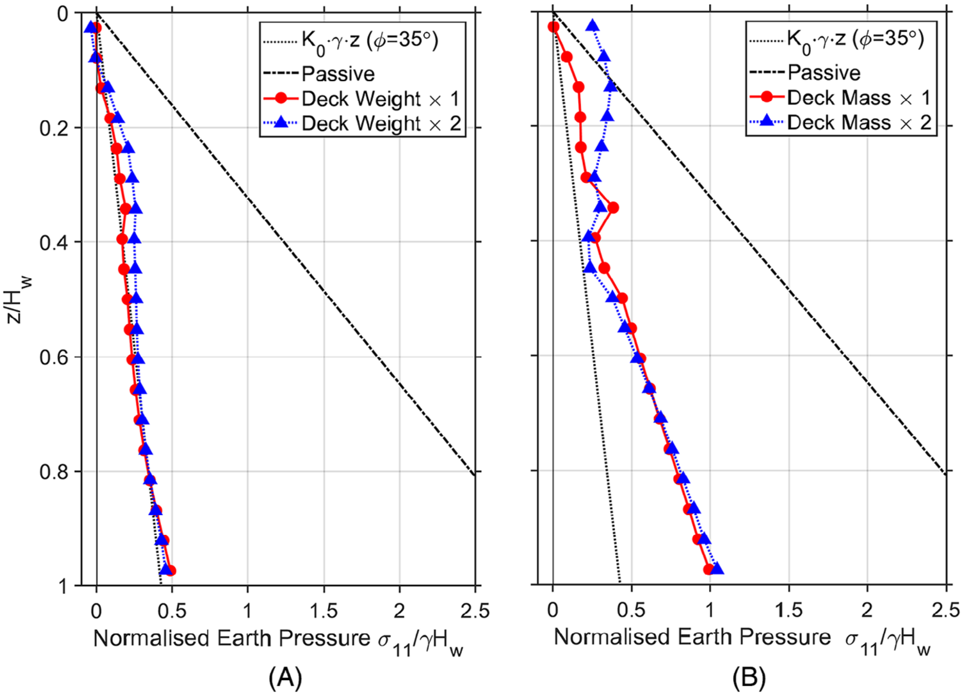

FIGURE 14 (A) Influence of the variation of the deck weight on static earth pressures behind the abutment wall: at-rest, and passive pressures versus numerical results at the end of the gravity analysis; (B) deck mass effect on the envelope of dynamic earth pressures behind the abutment wall, compared with at-rest and passive earth pressures.

the possible presence of a transition slab behind the wall. Furthermore, for some real bridge cases, it can be necessary to introduce a nonlinear model for the soil behavior (e.g., via pertinent 'p-y' springs in 2D) when large deck dimensions together with higher static and dynamic forces may induce non-linearities that cannot be faithfully modelled with the equivalent linear approximation.

5 | CONCLUSIONS

A numerical modelling technique in the open access finite-element platform OpenSees was adopted to simulate the earthquake response of a scaled physical model of an integral abutment bridge placed in a soil shear stack and tested as part of an EU/H2020-sponsored experimental campaign (SERA/SERENA) carried out at EQUALS Laboratory, University of Bristol. Out of the experimental configurations explored in the project, a benchmark setup without a compressible inclusion between soil and abutments and with the piles rigidly connected to the bridge foundation (pile cap) was selected to be numerically modelled, as a typical integral bridge system.

Particular attention was paid in modelling the interface between the soil and the integral abutments and piles. The up-to-date numerical model, developed in OpenSees, was capable of faithfully reproducing the acceleration measurements in the soil and the acceleration, displacements and bending strain measurements on the bridge model for a wide range of frequencies (reaching 50 Hz at model scale and approximately 50/5 = 10 Hz at prototype scale – see[47]). The increase in fundamental natural period of the bridge in the longitudinal direction due to SSI was found to be about 15%, which is considerable given the strong restraining action of the abutments. In particular, the matching in terms of frequency is very good both for the soil and the bridge system, with a maximum deviation of only 2% from measured values for the natural frequency of the bridge (about 40 Hz at model scale and approximately 40/5 = 8 Hz at prototype scale). Regarding accelerations, there is a very good match between the numerically predicted and measured values at the bottom of the soil container. The maximum discrepancy between acceleration peaks is around 40% and 60% at the top of the bridge and the top of the backfill, respectively. At the other locations, these discrepancies are on the order of 20%-30%, with the experimental and numerical values being slightly out of phase for the maximum peaks only. Also, the bending strains on the abutments show a reasonably good matching, with maximum discrepancies not exceeding 20% at the level of the pile cap.

The above good comparisons were achieved by modelling the problem in plane strain mode and using an equivalent-linear visco-elastic assumption for the soil response. A more detailed study on pile modelling would be required for improved simulations, as there are some differences between the measured and numerically predicted values due to the 3D nature of the response of the piles over the 2D modelling strategy adopted in this study. This extension, however, lies beyond the scope of this study.

The finite-element model provided dependable estimates of the static and dynamic earth pressures exerted on the abutment wall, which were not directly measured in the experimental campaign. The numerically computed earth pressures were compared to the predictions of two simplified, design-oriented procedures that are under consideration for inclusion in the new Eurocode 8 – Part 2 on Bridges. The comparison was deemed appropriate given that the scaling laws between the prototype and the model have been respected and the good matching between the numerically predicted and measured response. The earth pressures obtained with these formulations seem to be consistent with those obtained for the case presented herein if the abutment/foundation relative stiffness (parameter c) is evaluated by the numerical model, otherwise they are conservative if $c = 0.5$ is adopted. Moreover, the deck mass was found to have an important influence on the magnitude of the earth pressures as doubling the deck mass leads, as anticipated given the monolithic connection between the deck and the abutments, to a 50% increase in earth pressures close to the deck-abutment connection.

The numerical modelling strategy employed in this study could be advantageous over complex 3D models as it simplifies the boundary-value problem (notably the treatment of SSI effects) and can be applied to bridges of any dimensions. In real-life cases, the hypothesis of small soil strains and the associated equivalent-linear approximation adopted in this study should be verified on a case-by-case basis based on the expected seismic intensity level, and more advanced models should be adopted to capture the nonlinear soil behavior when the conditions adopted in this study do not hold.

Current practice in non-seismic design of IABs is to decouple the problem between the soil and the superstructure for predicting the earth pressures on the abutment into two separate sub-problems, while seismic codes such as the new EC8 propose simplified analytical approaches to evaluate earth pressures. The proposed modelling strategy informs further practice and can become a useful tool in investigating complex bridge configurations (e.g., long decks), allowing to obtain dependable estimates of earth pressures for serviceability limit states, whereas for cases closer to failure problem-specific modelling strategies using nonlinear soil models are likely to be necessary. Moreover, to extend the results of this study from model to prototype scale, additional numerical analyses of real-scale instrumented bridges adopting the proposed modelling strategy should be developed and evaluated against actual earthquake recordings and on-structure measurements.

ACKNOWLEDGEMENTS

This project has received funding from the European Union's Horizon 2020 research and innovation programme under the Marie Sklodowska-Curie grant agreement No. 892454 (https://cordis.europa.eu/project/id/892454). The experimental data were produced in EQUALS Lab, University of Bristol, as part of SERENA project (Seismic Response of Novel Integral Abutment-Bridges), funded by the EU/H2020 framework under grant agreement number 730900 (SERA). Camillo Nuti is grateful for the partial support by the ReLUIS Interuniversity Consortium as part of the agreement between ReLUIS and the Superior Council of Public Works (art.3 DM 578 of 17 December 2020 Ministry of Infrastructures); this publication does not necessarily reflect the Council's position and assessments. The authors would like to thank the reviewers for their comments which improved the quality of the paper.

DATA AVAILABILITY STATEMENT

The data that support the findings of this study are openly available at 10.5281/zenodo.13740030.

ORCID

Gabriele Fiorentino https://orcid.org/0000-0002-6444-0473
Raffaele De Risi https://orcid.org/0000-0002-5496-9656
Flavia De Luca https://orcid.org/0000-0003-2387-8580
George Mylonakis https://orcid.org/0000-0002-8455-8946
Bruno Briseghella https://orcid.org/0000-0002-8002-2298
Camillo Nuti https://orcid.org/0000-0002-0385-201X
Anastasios Sextos https://orcid.org/0000-0002-2616-9395

REFERENCES

1. Burke MP Jr. *Integral and Semi-Integral Bridges*. John Wiley & Sons; 2009.
2. Liu H, Han J, Parsons RL. Integral bridge abutments in response to seasonal temperature changes: state of knowledge and recent advances. *Front Built Environ*. 2022;8:916782.
3. Tatsuoka F, Tateyama M, Koda M, et al. Recent research and practice of GRS integral bridges for railways in Japan. *Jpn Geotech Soc Special Publ*. 2016;2(68):2307-2312.
4. Kang C, Schneider S, Wenner M, Marx S. Development of design and construction of high-speed railway bridges in Germany. *Eng Struct*. 2018;163:184-196.
5. DesRoches R, Muthukumar S. Effect of pounding and restrainers on seismic response of multiple-frame bridges. *J Struct Eng*. 2002;128(7):909-917.
6. AASHTO (American Association of State Highway and Transportation Officials). *Guide Specifications for LRFD Seismic Bridge Design*. 2nd ed. AASHTO; 2011.
7. BSI (British Standards Institution). *PD 6694-1:2011: Recommendations for the Design of Structures Subject to Traffic Loading to BS EN 1997-1*. BSI; 2011.
8. Cole RT, Rollins KM. Passive earth pressure mobilization during cyclic loading. *J Geotech Geoenviron Eng*. 2006;132(9):1154-1164.
9. Denton S, Riches O, Christie T, Kidd A. Developments in integral bridge design. *Bridge Design to Eurocodes: UK Implementation*. ICE Publishing; 2011:463-480.
10. Totaro A. Integral bridge design from the UK Highways perspective, COMPDYN 2019. In 7th ECCOMAS Thematic Conference on Computational Methods in Structural Dynamics and Earthquake Engineering, Crete, Greece; (24-26 June 2019).
11. Mononobe N, Matsuo M. Experimental Investigation of Lateral Earth Pressure during Earthquakes. Earthquake Research Institute and Research Office of Public Works; 1932: 884-902.
12. Okabe S. General theory of earth pressure and seismic stability of retaining wall and dam. *J Jpn Soc Civil Eng*. 1924;10(6):1277-1323.
13. Anderson DG, Martin GR, Lam I, Wang JN. *Seismic Analysis and Design of Retaining Walls, Buried Structures, Slopes, and Embankments*. Transportation Research Board; 2009. NCHRP Rep. 611.
14. Brandenberg SJ, Mylonakis G, Stewart JP. Kinematic framework for evaluating seismic earth pressures on retaining walls. *J Geotech Geoenviron Eng*. 2015;141(7):04015031.
15. Kloukinas P, di Santolo AS, Penna A, et al. Investigation of seismic response of cantilever retaining walls: limit analysis vs shaking table testing. *Soil Dyn Earthq Eng*. 2015;77:432-445.
16. Mylonakis G, Kloukinas P, Papantonopoulos C. An alternative to the Mononobe–Okabe equations for seismic earth pressures. *Soil Dyn Earthq Eng*. 2007;27(10):957-969.
17. Sherif MA, Fang YS. Dynamic earth pressures on walls rotating about the top. *Soils Found*. 1984;24(4):109-117.
18. CEN (European Committee for Standardization). Eurocode 8. Design of structures for earthquake resistance—Part 2: bridges, Brussels, Belgium; 2005.
19. CEN (European Committee for Standardization). Eurocode 8. Design of structures for earthquake resistance—Part 2: bridges. In: Technical Committee 250, Sub-Committee 8, Technical report N1182. CEN; 2022a.
20. Frosch RJ, Kreger ME, Talbott AM, Earthquake Resistance of Integral Bridges. Joint Transportation Research Program, FHWA/IN/JTRP-2008/11, SPR-2867; 2009.
21. Kozak DL, LaFave JM, Fahnestock LA. Seismic modeling of integral abutment bridges in Illinois. *Eng Struct*. 2018;165:170-183.
22. Ni Choine M, Kashani M, Lowes LN, et al. Nonlinear dynamic analysis and seismic fragility assessment of a corrosion damaged integral bridge. *Int J Struct Integr*. 2016;7(1):31-43.
23. Zhang Y, Conte JP, Yang Z, Elgamal A, Bielak J, Acero G. Two-dimensional nonlinear earthquake response analysis of a bridge-foundation-ground system. *Earthquake Spectra*. 2008;24(2):343-386. 120.
24. Computers and Structures. SAP2000. Version 24. Computers and Structures, Inc.; 2023.
25. Franchin P, Pinto PE. Performance-based seismic design of integral abutment bridges. *B Earthq Eng*. 2014;12:939-960.
26. Mahjoubi S, Maleki S. Finite element modelling and seismic behaviour of integral abutment bridges considering soil-structure interaction. *Eur J Environ Civ Eng*. 2020;24(6):767-786. doi:10.1080/19648189.2017.1421483
27. Vasheghani-Farahani R, Zhao Q, Burdette EG. Seismic analysis of integral abutment bridge in Tennessee, including soil-structure interaction. *Transp Res Rec*. 2010;2201(1):70-79.
28. LaFave JM, Fahnestock L, Kozak DL. Seismic performance of integral abutment highway bridges in Illinois (No. FHWA-ICT-18-012). Illinois Center for Transportation; 2018.
29. Dicleli M, Erhan S. Effect of foundation soil stiffness on the seismic performance of integral bridges. *Struct Eng Int*. 2011;21(2):162-168.
30. Marchi A, Gallese D, Gorini DN, Franchin P, Callisto L. On the seismic performance of straight integral abutment bridges: from advanced numerical modelling to a practice-oriented analysis method. *Earthquake Eng Struct Dyn*. 2023;52(1):164-182. doi:10.1002/eqe.3452
31. Marchi A, Franchin P. Equivalent static methods for seismic design of straight integral abutment bridges. *Earthquake Eng Struct Dyn*. 2023;53(3):1048-1066.
32. Gallese D, Gorini DN, Callisto L. A nonlinear static analysis for the seismic design of single-span integral abutment bridges. *Géotechnique*. 2023:1-15. 10.1680/jgeot.22.00229
33. Mitoulis SA, Palaiochorinou A, Georgiadis I, Argyroudis S. Extending the application of integral frame abutment bridges in earthquake-prone areas by using novel isolators of recycled materials. *Earthquake Eng Struct Dyn*. 2016;45(14):2283-2301.

34. Tsinidis G, Papantou M, Mitoulis S. Response of integral abutment bridges under a sequence of thermal loading and seismic shaking. *Earthquakes Struct*. 2019;16(1):11.
35. Xu M, Liu P. Response of full-height frame integral abutments subjected to seismic motions. *Soil Dyn Earthq Eng*. 2019;121:356-368.
36. Seid-Karbasi M, Fernando V. Numerical assessment of seismic earth pressures for integral abutment bridges. In: Geo-Congress 2019. Earthquake engineering and soil dynamics: selected papers from sessions of the Eighth International Conference on Case Histories in Geotechnical Engineering, Philadelphia, Pennsylvania (March 24-27, 2019). ASCE book series.
37. Ng C, Springman S, Norrish A. Soil-structure interaction of spread-base integral bridge abutments. *Soils Found*. 1998;38(1):145-162.
38. Al-Qarawi A, Leo C, Liyanapathirana DS. Effects of wall movements on performance of integral abutment bridges. *Int J Geomech*. 2020;20(2):04019157.
39. Arsoy S. Mobilization of passive earth pressures behind abutments of jointless bridges. *Transp Res Rec*. 2004;1868(1):199-204.
40. Bloodworth AG, Xu M, Banks JR, Clayton CR. Predicting the earth pressure on integral bridge abutments. *J Bridge Eng*. 2012;17(2):371-381.
41. Faraji S, Ting JM, Crovo DS, Ernst H. Nonlinear analysis of integral bridges: finite-element model. *J Geotech Geoenviron Eng*. 2001;127(5):454-461.
42. Lehane BM. Lateral soil stiffness adjacent to deep integral bridge abutments. *Géotechnique*. 2011;61(7):593-603.
43. Luo S, De Luca F, De Risi R, et al. Challenges and perspectives for integral bridges in the UK: from design practice to fieldwork through small-scale laboratory experiments. Proc Inst Civ Eng -Smart Infrastruct Construct. 2022;175(1):27-43.
44. Luo S, Huang Z, Asia Y, et al. Physical and numerical investigation of integral bridge abutment stiffness due to seasonal thermal loading. *Transport Geotech*. 2023;42:101064.
45. Muir Wood D, Nash D. Earth pressures on an integral bridge abutment: a numerical case study. *Soils Found*. 2000;40(6):23-38. doi:10.3208/sandf.40.6_23
46. Perić D, Miletić M, Shah BR, Esmaeily A, Wang H. Thermally induced soil structure interaction in the existing integral bridge. *Eng Struct*. 2016;106:484-494.
47. Fiorentino G, Cengiz C, De Luca F, et al. Integral abutment bridges: investigation of seismic soil-structure interaction effects by shaking table testing. *Earthquake Eng Struct Dyn*. 2021;50(6):1517-1538.
48. Lings ML, Dietz MS. An improved direct shear apparatus for sand. *Géotechnique*. 2004;54(4):245-256.
49. Luzi L, Lanzano G, Felicetta C, et al. Engineering Strong Motion Database (ESM) (Version 2.0). Istituto Nazionale di Geofisica e Vulcanologia (INGV); 2020. doi:10.13127/ESM.2
50. Hashash YMA, Musgrove MI, Harmon JA, Groholski DR, Phillips CA, Park D. *DEEPSOIL 6.1. User Manual*. Department of Civil and Environmental Engineering University of Illinois at Urbana-Champaign; 2016.
51. Simulia. Abaqus. Version 2021. Dassault Systèmes; 2021.
52. Huang X, Kwon OS, Kwon TH. An integrated simulation method for soil-structure interaction analysis of nuclear structures. *Earthquake Eng Struct Dyn*. 2021;50(10):2634-2652.
53. Ramirez J, Barrero AR, Chen L, et al. Site response in a layered liquefiable deposit: evaluation of different numerical tools and methodologies with centrifuge experimental results. *J Geotech Geoenviron Eng*. 2018;144(10):04018073.
54. Requena-Garcia-Cruz MV, Bento R, Durand-Neyra P, Morales-Esteban A. Analysis of the soil structure-interaction effects on the seismic vulnerability of mid-rise RC buildings in Lisbon. *Structures*. 2022;38:599-617.
55. McKenna F. OpenSees: a framework for earthquake engineering simulation. *Comput Sci Eng*. 2011;13(4):58-66.
56. Petek KA. *Development and Application of Mixed Beam-Solid Models for Analysis of Soil-Pile Interaction Problems*. University of Washington; 2006.
57. Petracca M, Candeloro F, Camata G. STKO User Manual. *ASDEA Software Technology*; 2020.
58. Bathe KJ. Conserving energy and momentum in nonlinear dynamics: a simple implicit time integration scheme. *Comput Struct*. 2007;85(7-8):437-445.
59. McGann CR, Arduino P. Numerical assessment of the influence of foundation pinning, deck resistance, and 3D site geometry on the response of bridge foundations to demands of liquefaction-induced lateral soil deformation. *Soil Dyn Earthq Eng*. 2015;79:379-390.
60. McGann CR, Arduino P. Numerical assessment of three-dimensional foundation pinning effects during lateral spreading at the Mataquito River bridge. *J Geotech Geoenviron Eng*. 2014;140(8):04014037.
61. McGann CR, Arduino P, Mackenzie-Helnwein P. Applicability of conventional p-y relations to the analysis of piles in laterally spreading soil. *J Geotech Geoenviron Eng*. 2011;137(6):557-567.
62. Jardine RJ, Lehane BM, Everton SJ. Friction coefficients for piles in sands and silts. In: Offshore Site Investigation and Foundation Behaviour: Papers presented at a conference organised by the Society for Underwater Technology and held in London, UK, September 22–24, 1992. Springer; 1993:661-677.
63. Veletsos AS, Younan AH. Dynamic response of cantilever retaining walls. *J Geotech Geoenviron Eng*. 1997;123(2):161-172.
64. Trifunac MD, Todorovska MI, Ivanović SS. Peak velocities and peak surface strains during Northridge, California, earthquake of 17 January 1994. *Soil Dyn Earthquake Eng*. 1996;15(5):301-310.
65. Ochmański M, Mašín D, Duque J. An approach for 2D modelling of laterally loaded piles. *Soils Found*. 2023;63(1):101263.
66. Psyrras N, Sextos A, Crewe A, Dietz M, Mylonakis G. Physical modeling of the seismic response of gas pipelines in laterally inhomogeneous soil. *J Geotech Geoenviron Eng*. 2020;146(5):04020031.
67. Lysmer J, Kuhlemeyer RL. Finite dynamic model for infinite media. *J Eng Mech*. 1969;95:859-878.

68. Cavalieri F, Correia AA, Pinho R. Comparative nonlinear soil-structure interaction analyses using macro-element and soil-block modelling approaches. *Bull Earthquake Eng*. 2022;20(7):3295-3328.
69. Kramer SL. *Geotechnical Earthquake Engineering*. Prentice Hall; 1996.
70. Yoshida N. *Seismic Ground Response Analysis*. Springer; 2015.
71. Itasca. FLAC3D. *Fast Lagrangian Analysis of Continua in 3-Dimensions, Version 6.0;* 2020.
72. Volpini C, Douglas J, Nielsen AH. Guidance on conducting 2D linear viscoelastic site response analysis using a finite element code. *J Earthquake Eng*. 2019;25(6):1153-1170.
73. Madera GA. Fundamental Period and Amplification of Peak Acceleration in Layered Systems. Research Report R70-37, Dept. of Civil Engineering, MIT., Cambridge, Mass; 1970.
74. Chidichimo A, Cairo R, Dente G, Taylor CA, Mylonakis G. 1-g Experimental investigation of bi-layer soil response and kinematic pile bending. *Soil Dyn Earthq Eng*. 2014;67:219-232.
75. Durante MG, Karamitros D, Di Sarno L, et al. Characterisation of shear wave velocity profiles of non-uniform bi-layer soil deposits: analytical evaluation and experimental validation. *Soil Dyn Earthq Eng*. 2015;75:44-54.
76. Crewe AJ, Lings ML, Taylor CA, Yeung AK, Andrighetto R. Development of a large flexible shear stack for testing dry sand and simple direct foundations on a shaking table. In: Fifth SECED Conference on European Seismic Design Practice; 1995:163-168. Routledge.
77. Ghayoomi M, Dashti S, McCartney JS. Performance of a transparent Flexible Shear Beam container for geotechnical centrifuge modeling of dynamic problems. *Soil Dyn Earthq Eng*. 2013;53:230-239.
78. Kim S, Stewart JP. Kinematic soil-structure interaction from strong motion recordings. *J Geotech Geoenviron Eng*. 2003;129(4):323-335.
79. Dreier D, Burdet O, Muttoni A. Transition slabs of integral abutment bridges. *Struct Eng Int*. 2011;21(2):144-150.
80. Liu H, Han J, Parsons RL. Geosynthetic reinforcement of backfill behind integral abutments to mitigate approach slab distresses. *Eng Struct*. 2022;269:114772.
81. Crispin JJ. *Static and Dynamic Analysis of Piles in Inhomogeneous Soil*. PhD Dissertation, Department of Civil Engineering, University of Bristol; 2022.
82. Mylonakis G. *Contribution to Static and Seismic Analysis of Piles and Pile-Supported Bridge Piers*. Ph.D. Dissertation, Department of Civil Engineering, State University of New York at Buffalo; 1995.
83. Agapaki E, Karatzia X, Mylonakis G, Higher-order Winkler solutions for laterally loaded piles. In: Proceedings of the 16th European Conference on Earthquake Engineering. European Association for Earthquake Engineering (EAEE); 2018:18-21.
84. Klar A, Frydman S. Three-dimensional analysis of lateral pile response using two-dimensional explicit numerical scheme. *J Geotech Geoenviron Eng*. 2022;128(9):775-784.
85. Mylonakis G, Gazetas G. Lateral vibration and internal forces of grouped piles in layered soil. *J Geotech Geoenviron Eng*. 1999;125(1):16-25.
86. Sluis J, Besseling F, Stuurwold P. *Modelling of a Pile Row in a 2D Plane Strain FE-Analysis*; 2014:277-282.
87. Bentley Systems, Inc. PLAXIS 2D. Version 22. Bentley Systems, Inc.; 2022.
88. Li G, Motamed R. Finite element modeling of soil-pile response subjected to liquefaction-induced lateral spreading in a large-scale shake table experiment. *Soil Dyn Earthq Eng*. 2017;92:573-584.
89. Kim Y, Jeong S. Analysis of soil resistance on laterally loaded piles based on 3D soil–pile interaction. *Comput Geotech*. 2011;38(2):248-257.
90. Feldmann M, Naumes J, Pak D, et al. INTAB DG eng 02 Design guide Integral bridges, Economic and Durable Design of Composite Bridges with Integral Abutments. CEN/TC 250/SC 10, EN 1990 Basis of structural design; 2010. Accessed September 2024. https://data.europa.eu/doi/10.2777/91014
91. Lancellotta R. Lower-bound approach for seismic passive earth resistance. *Géotechnique*. 2007;57(3):319-321.
92. Rampello S, Callisto L, Masini L. Spinta delle terre sulle strutture di sostegno. In: Opere di sostegno e di stabilizzazione dei pendii, Conferenze di Geotecnica di Torino, XXIII ciclo; 2011:1–45 (in Italian).
93. CEN (European Committee for Standardization). Eurocode 8. Design of structures for earthquake resistance—Part 5: Geotechnical aspects, foundations, retaining and underground structures. Technical Committee 250, Sub-Committee 8, Technical Report N1143. CEN; 2022b.
94. Kloukinas P, Mylonakis G. Generalized Rankine solutions for seismic earth pressures: validity, limitations & refinements. *Soil Dyn Earthq Eng*. 2014;179:10852.
95. Agapaki E. *Higher-Order Winkler Analytical Solutions of Flexible Piles and Walls*. Diploma Thesis. University of Patras; 2014.

How to cite this article: Fiorentino G, De Risi R, De Luca F, et al. SSI-induced seismic earth pressures on an integral abutment bridge model: Experimental measurements versus numerical simulations and code provisions. *Earthquake Engng Struct Dyn*. 2024;53:4830–4852. https://doi.org/10.1002/eqe.4237